

2
3 **PI3K-Yap activity drives cortical gyrification and hydrocephalus in**
4 **mice**

5
6 Achira Roy¹, Rory M. Murphy¹, Mei Deng², James W. MacDonald³, Theo K. Bammler³,
7 Kimberly A. Aldinger^{1,2}, Ian A. Glass², Kathleen J. Millen^{1,2*}

8
9 ¹Center for Integrative Brain Research, Seattle Children's Research Institute, Seattle,
10 Washington, USA; ²Division of Genetic Medicine, Department of Pediatrics, University
11 of Washington, Seattle, Washington, USA; ³Department of Environmental and
12 Occupational Health Sciences, School of Public Health, University of Washington,
13 Seattle, Washington, USA

14
15 *Correspondence: Kathleen J. Millen

16 Seattle Children's Research Institute

17 JMB 10 - Center for Integrative Brain Research

18 1900 9th Avenue, Seattle, WA 98101

19 Email: kathleen.millen@seattlechildrens.org

20 Tel: +1-206-884-3225

Competing Interests Statement: All authors read and approved the final manuscript.
None of the authors have competing interests.

Short Title: PI3K-Yap signaling drives mouse cortical gyrification

Keywords: PI3K; cortical gyrification; critical period; hydrocephalus; Yap

Number of Figures: 8

Number of Figure supplements: 12

Number of Videos: 2

Number of Source Data files: 2

ABSTRACT

Mechanisms driving the initiation of brain folding are incompletely understood. We have previously characterized mouse models recapitulating human *PIK3CA*-related brain overgrowth, epilepsy, dysplastic gyrification and hydrocephalus (Roy et al., 2015). Using the same, highly regulatable brain-specific model, here we report PI3K-dependent mechanisms underlying gyrification of the normally smooth mouse cortex, and hydrocephalus. We demonstrate that a brief embryonic *Pik3ca* activation was sufficient to drive subtle changes in apical cell adhesion and subcellular Yap translocation, causing focal proliferation and subsequent initiation of the stereotypic ‘gyrification sequence’, seen in naturally gyrencephalic mammals. Treatment with verteporfin, a nuclear Yap inhibitor, restored apical surface integrity, normalized proliferation, attenuated gyrification and rescued the associated hydrocephalus, highlighting the interrelated role of regulated PI3K-Yap signaling in normal neural-ependymal

44 development. Our data defines apical cell-adhesion as the earliest known substrate for
45 cortical gyrification. In addition, our preclinical results support the testing of Yap-related
46 small-molecule therapeutics for developmental hydrocephalus.

INTRODUCTION

The mammalian brain has evolved through multiple transitions between gyrencephaly and lissencephaly (Lewitus et al., 2014). Cortical expansion and gyrification have been implicated in the evolution of human cognition; and dysplastic gyrification is associated with numerous neurodevelopmental disorders including hydrocephalus (Jimenez et al., 2014, Guerra et al., 2015, Gregory et al., 2016, Parrini et al., 2016, Borrell, 2018). Yet, despite the high significance, the mechanisms which create a smooth or folded brain remain poorly understood.

In vivo mouse and ferret studies together with *in vitro* human organotypic slice analyses have identified several genetic, cell biological and biomechanical factors that contribute to gyrification (Borrell, 2018, Llinares-Benadero and Borrell, 2019). Stereotypic, *bona fide* cortical folding includes formation of gyri (away from ventricle) and sulci (proximal to ventricle) of differential thickness (gyri thicker than the sulci), adjacent to a predominantly unfolded apical ventricular lining (Borrell, 2018). Naturally gyrencephalic species undergo a sequence of developmental events referred to here as the “gyrification sequence”. It begins with apical progenitor proliferation followed by differential expansion of secondary progenitors, comprising of intermediate precursors (IPs) and basal radial glia cells (bRGs). The expansion of progenitors is associated with focal modes of neuronal differentiation, and migration that is mediated by variable ECM stiffness (Borrell, 2018, Llinares-Benadero and Borrell, 2019). Although differential progenitor expansion is central to gyrification, little is known about the initiating steps of this highly regulated process (Gregory et al., 2016).

We previously generated mice with activating mutations of *Pik3ca*, the catalytic subunit of the phosphoinositide 3-kinase (PI3K) enzyme, to model human brain overgrowth syndromes including megalencephaly and epilepsy (Roy et al., 2015). Since dysplastic cortical folding and developmental hydrocephalus are within the spectrum of PI3K-related brain overgrowth syndromes (Mirzaa et al., 2012, Keppler-Noreuil et al., 2014, Jansen et al., 2015), we have now used our tet-inducible activating *Pik3ca*^{H1047R} mutant mice (Roy et al., 2015) to study mechanisms underlying these additional phenotypes. Hydrocephalus, affecting approximately 1 in 1000 births, is among the most common neurodevelopmental disorders with often devastating outcome (Guerra et al., 2015, Tully et al., 2016). It is characterized by abnormal expansion of brain ventricles (ventriculomegaly) and progressive accumulation of cerebrospinal fluid (Jimenez et al., 2014, Guerra et al., 2015). New therapeutic approaches are urgently needed since current treatment requires invasive surgeries with associated significant complications (Khan et al., 2015). PIK3CA-related hydrocephalus is a subtype of developmental hydrocephalus, caused by disrupted brain development associated with genetic abnormalities (Tully and Dobyns, 2014, Tully et al., 2016). Infantile hydrocephalus can also result from environmental insult, including intra-ventricular hemorrhage associated with prematurity (Adamsbaum et al., 1998, Jimenez et al., 2009). Despite identification of several contributing factors, the underlying cellular and molecular mechanisms that cause hydrocephalus remain largely unknown.

Here we report that *Pik3ca* activation in embryonic cortical progenitors during a critical two-day period was sufficient to drive cortical gyrification in mice. PI3K activation disrupted apical junctions and caused ectopic subcellular translocation of Yap leading

to neural proliferation and gyrification, as well as abnormal ependymal development and hydrocephalus. Both the gyrification and hydrocephalus phenotypes were attenuated in the mutant mice by treatment with verteporfin (report, 2000, Schmidt-Erfurth and Hasan, 2000, Liu-Chittenden et al., 2012), a nuclear Yap inhibitor.

These results demonstrate that the PI3K/Hippo-Yap pathway is finely tuned to regulate cell adhesion and proliferation along the apical lining of the forebrain to maintain the lissencephalic mouse brain. Subtle alterations in this pathway during the mid-neurogenic phase have dramatic consequences for the cytoarchitecture of forebrain ventricular linings and the interrelated processes of neurogenesis, gyrification and ependymal development.

RESULTS

***Pik3ca* activating mutations caused gyrification of the normally lissencephalic mouse cortex**

We identified striking gyrification of the hippocampus and neocortex in the embryonically induced *GFAP-cre;Pik3ca*^{H1047R} mutant mice (**Figure 1a-l**; (Roy et al., 2015)) This mutant also recapitulates human PI3K-related developmental hydrocephalus, without any evidence of stenosis along the antero-posterior extent of the brain. In this model, a transgene encoding an activating *H1047R* mutation in the human *PIK3CA* gene has dual spatio-temporal regulation, such that the presence of both *cre* protein and doxycycline is required to activate the mutation in **cre**-positive neuronal progenitors (**Figure 1 – figure supplement 1a,b**) (Roy et al., 2015). The *GFAP-cre* driver used in this study gets activated in neural progenitors at around embryonic day (E)13 (Zhuo et al., 2001, Roy et al., 2015). Around this early activation time, this *cre* line demonstrates a strong high-medial-low-lateral expression gradient in the forebrain, as well as an apical-low-basal-high gradient within the lateral neocortex, as seen at E14.5 (**Figure 1 – figure supplement 1c**). These differential gradients decrease gradually with the progression of developmental age (**Figure 1 – figure supplement 1d**). Embryonically induced postnatal (P)3 *GFAP-cre;Pik3ca*^{H1047R} mutants (doxycycline: E0.5>P3) demonstrated highly convoluted medial tissue, with indistinct hippocampal morphology (**Figure 1b,d,f**) (Roy et al., 2015). This hippocampal folding phenotype was 100% penetrant with stereotypic gyral pattern in all mutants (n>50) studied. 3-D models of P3 control and mutant hippocampi clearly demonstrate the differential anatomical features (**Video 1, Video 2**; still images in **Figure 1e,f**). Ventriculomegaly, indicating

developing hydrocephalus, was also clearly evident in all of the mutant brains, seen from as early as E14.5 (**Figure 1b,d; Figure 1 – figure supplement 2f,p-s; Figure 1 – figure supplement 3a,c,e**). Less pronounced lateral neocortical folding was also evident with 100% penetrance, although variable in position (**Figure 1b,d; Figure 1 – figure supplement 2f-i**). Both neocortical and hippocampal folds in the *Pik3ca*^{H1047R} mutant mice followed the criteria of *bona fide* cortical gyrification (Borrell, 2018): a) folded pial surface and underlying layers, b) predominantly smooth apical surfaces adjacent to the lateral ventricle, c) differential thickness between gyri and sulci (**Figure 1 – figure supplement 2f-i, p-s**). Notably, similar lateral and medial cortical gyrification was also documented in mice with *Pik3ca*^{H1047R} mutation activated by *Emx1-cre* (D'Gama et al., 2017). Together, these data demonstrate that *Pik3ca* activation is sufficient to cause cortical gyrification across the entire mouse dorsal telencephalon with the phenotype likely dependent on the time and regional gradients of *cre* activity, and regional differences in neurogenic periods.

Focal increases in progenitors initiated *bona fide* cortical gyrification in *Pik3ca*^{H1047R} mutant

To determine if *Pik3ca*^{H1047R} mice modeled *bona fide* cortical gyrification seen in naturally gyrified mammals (Borrell, 2018), we assessed neural patterning and progenitor proliferation during embryogenesis. We focused on the developing hippocampus, where gyrification was most prominent in pattern and location. P3 *Pik3ca*^{H1047R} mutants showed normally patterned subdivisions of hippocampus proper (CA1-4) and dentate gyrus (DG; **Figure 1g-l**). Similar to the control littermates, *Ctip2*

expression was high in the mutant CA1 and DG, sparse in CA2 and absent in Tbr1⁺ CA3. Ctip2 expression also revealed that the gyrification in mutants was primarily restricted to CA1, with possibly secondary folding evident in the DG. The *Pik3ca* activating mutation resulted in a significant increase in the lengths of P3 CA field (p<0.0001) and dentate gyrus (p=0.03), compared to the respective controls (**Figure 1 – figure supplement 3a,b**). The first visual sign of reproducible cortical folding was observed at E16.5 in the *Pik3ca*^{H1047R} mutant dorso-lateral neocortex (**Figure 1 – figure supplement 3e**).

Further histological analyses confirmed that *GFAP-cre;Pik3ca*^{H1047R} mutants replicated the coordinated neurogenic sequence seen in gyrencephalic mammals. Compared with control, both E14.5 and E16.5 mutants had significantly longer medial ventricular linings (p=0.0028 and p<0.0001 respectively; **Figure 1 – figure supplement 3c-f**), suggesting early expansion of apical progenitors. Short BrdU pulse confirmed significantly higher proliferation (p<0.05) in mutants at E14.5, but not at E16.5, compared to respective controls (**Figure 2b-e**). Sox2⁺ primary progenitors in the mutant CA1 ventricular-subventricular zone were significantly increased at E14.5 (p<0.05) and decreased at E16.5 (p<0.01). Tbr2⁺ IPs were unchanged at E14.5; but significantly increased at E16.5 (p<0.05), demonstrating a gradual increase in secondary progenitor pool *in lieu* of the primary progenitors (**Figure 2f-i**). This trend of higher progenitor number was maintained even postnatally, especially in the mutant gyral ventricular-subventricular zone (**Figure 2l-m'**). The number of Sox2⁺Tbr2⁻ bRGs in outer subventricular zone was not significantly different between control and mutant at E16.5

(**Figure 2i**). The mutant CA1 further demonstrated significantly higher neuronal differentiation at E16.5 (**Figure 2j,k**).

Birth-dating analysis showed normal neuronal fate specification in P0 mutant CA1 (**Figure 2 – figure supplement 1a-c**). Although the mutant hippocampal subdivisions were grossly intact, there were minor migration defects as evidenced by a loosely packed *stratum pyramidale* (PL), reduced *stratum lacunosum-moleculare* (*slm*), and scattered Calbindin⁺ pyramidal cell subtype in the gyral white matter (**Figure 2l',m'**; **Figure 2 – figure supplement 1f-i,k,l**). Similar to our report of the neocortical phenotype (Roy et al., 2015), we observed a disrupted Nestin⁺/GFAP⁺ radial glial scaffold throughout mouse embryogenesis, starting as early as E14.5 (**Figure 2 – figure supplement 1d-i**). A divergent fiber distribution was evident postnatally at each gyrus, similar to that seen in naturally gyrencephalic species (**Figure 2n-o'**) (Fernandez et al., 2016, Borrell, 2018). Focally concentrated progenitor cells found in the P3 gyral ventricular-subventricular zone and the funneling effect of radial glial scaffold fibers most certainly amplified the earlier developmental disruptions leading to *bona fide* gyrification of the normally lissencephalic cortex.

***Pik3ca* mutation-driven gyrification in mice had a short embryonic critical period**

Although numerous mouse models of cortical gyrification exist, our highly regulatable model is an extremely valuable tool to dissect fundamental molecular mechanisms. Specifically, via temporally restricted doxycycline administration, we generated a time-series of *GFAP-cre;Pik3ca*^{H1047R} mutants to begin to dissect mechanisms underlying gyrification and other phenotypes (**Figure 3b-d,f-i**). Consistent

with our previous study (Roy et al., 2015), postnatal induction of *Pik3ca*^{H1047R} allele failed to cause overtly abnormal brain morphology (**Figure 3i**). By contrast, doxycycline induction from either E0.5 or E13.5 generated the most severely gyrified CA1 with identical stereotypic pattern (**Figure 3b-d,k**). This was not unexpected since despite doxycycline availability, the *cre* protein was produced in neural progenitors only from ~E13 (Roy et al., 2015). *Pik3ca*-related ventriculomegaly resulted broadly from mutation induction at any embryonic time point (**Figure 1b,d; Figure 1 – figure supplement 2f,p; Figure 1 – figure supplement 3a,c,e; Figure 3b-d,f-h; Figure 3 – figure supplement 1c**).

Remarkably, a short 2-day window of doxycycline administration from E13.5 to (>) E15.5 was sufficient to completely recapitulate the highly stereotypic gyrification pattern seen in mutants with constitutive administration of doxycycline throughout development. Despite the identical gyrification pattern, the CA1 PL of P3 (doxycycline: E13.5>E15.5) mutant was more compact than that of the constitutively activated mutants, suggesting a later role for activated *Pik3ca* in regulating the minor neuronal migration abnormalities detected in this model. Shorter periods of doxycycline treatment (E13.5>E14.5, E14.5>E15.5) within this critical period did not result in gyrification, despite mild cortical dysplasia and ventriculomegaly (**Figure 3 – figure supplement 1b-e**). Induction beyond E15.5 (E15.5>P3, E15.5>E17.5, E17.5>P0) caused a gradual attenuation of the gyrification phenotype and significantly smaller CA1 PL lengths in the respective P3 mutants (**Figure 3f-h,k; Figure 3 – figure supplement 1a**). To further define gyrification mechanisms, we therefore focused our analysis of developmental events using minimally induced (doxycycline E13.5>E15.5) mutant mice.

Disordered junctional proteins at embryonic ventricular lining were the earliest presage of the mutant gyrification phenotype

The first obvious morphological sign of CA1 gyrification in minimally induced (doxycycline E13.5>E15.5) mutants was a medial “ripple” at E17.5 (**Figure 3 – figure supplement 1f-n**). This was accompanied by dispersed radial glial fibers, loosely packed Ctip2⁺ PL with ectopic Calbindin⁺ cells, as well as reduced *s/m* marked by cell adhesion molecule L1 (**Figure 3 – figure supplement 1o-v**). Since these phenotypes suggested that neuronal migration abnormalities might underlie the gyrification phenotype, we investigated localization of ECM protein Reelin in the *Pik3ca*^{H1047R} mutant. Reelin is well-known for its role in cell migration; and its expression in Cajal-Retzius cells is typically required to direct normal lamination of pyramidal neurons in the development of CA fields (D'Arcangelo et al., 1995). Further, ectopic Reelin has been reported to contribute to cortical dysplasia in another PI3K pathway overactivation mouse model (Baek et al., 2015). However, we found no evidence of ectopic Reelin⁺ cells in either E17.5 or P2 mutant CA1 regions (**Figure 2 – figure supplement 1m,n; Figure 3 – figure supplement 1r,v**).

Focal increases in proliferation observed at the mutant ventricular-subventricular zone suggested that disruptions at the apical (ventricular) linings were fundamental to the gyrification phenotype. In control E16.5 and P3 mice, the neocortical and hippocampal ventricular linings are tightly juxtaposed (**Figure 4b-e, Figure 4 – figure supplement 1b-d**). The normal juxtaposition of apical membranes was disrupted in E16.5 mutants, leading to the formation of loose gaps/bubbles along the edge (**Figure**

239 **4f-i)**, which eventually resulted in completely unzipped ventricular linings postnatally
240 **(Figure 4 – figure supplement 1e-j)**. Junctional proteins delineating the ventricular
241 surface, including β -Catenin, N-Cadherin, ZO-1 (Kadowaki et al., 2007), were focally
242 discontinuous and often ectopic in P3 mutants, compared to their littermate controls.
243 Milder, yet clear disruptions of cell polarity were observed at E16.5 and E14.5 at the
244 mutant medial apical membrane **(Figure 4f-i,o-r)**.

245
246 **Focal increases in nuclear Yap (nYap) and neural progenitors at the mutant**
247 **ventricular edge corresponded to gyrification zones**

248 Forebrain ependymal development is normally initiated in mouse during mid-
249 gestation (Jimenez et al., 2014). Our analysis of ependymal markers (Yap, Vimentin,
250 Six3) indicated clear abnormalities in mutant mice (Schnitzer et al., 1981, Lavado and
251 Oliver, 2011, Park et al., 2016). Especially striking were alterations in the localization of
252 Yap, a molecule that sits at the nexus of multiple signaling pathways and that is
253 normally expressed in blood vessels and at the ZO1⁺ apical membrane of differentiating
254 ependymal cells **(Figure 5b,c,o-p,s,s')**. At P3, numerous ectopic Yap⁺ cells were
255 distributed distal to the mutant CA1 ventricular edge, particularly predominant in the
256 developing gyri **(Figure 5e,i,m)**. At E16.5, we observed focal concentrations of Yap⁺
257 cells in the unzipped areas of the mutant ventricular lining; subtle focal disruption was
258 evident as early as E14.5 **(Figure 5q,t)**. Notably, Yap localization was cytoplasmic
259 (cYap) and apical at all stages in control mice. In mutants however, we observed
260 aberrant nuclear localization of Yap at all stages, especially evident at P3. The total
261 number of nYap⁺ cells is significantly higher in P3 mutant sulcus and gyrus, compared

with the controls ($p < 0.0001$, **Figure 5I**). Magnified images of E16.5 and E14.5 mutant apical edges displayed a more frequent presence of nYap⁺ cells, compared to the respective controls (**Figure 5 o',q',s',t'**). Disruption of ependymal development was also supported by altered expression of Vimentin and Six3 expression in the mutant (**Figure 5d,h,k; Figure 5 – figure supplement 1a-d**).

Inhibition of nYap attenuated gyrification and rescued ventriculomegaly

In neural stem cells, nYap drives proliferation and cYap acts to stabilize apical adherens junctions (Park et al., 2016, Lavado et al., 2018). We therefore hypothesized that focal nuclear mis-localization of Yap, from cytoplasm to nucleus, in the early mutant ventricular zone, drives focal over-proliferation and disrupts apical cell adhesion at nascent mutant gyri. To test this hypothesis, we administered nYap inhibitor verteporfin (report, 2000, Schmidt-Erfurth and Hasan, 2000, Liu-Chittenden et al., 2012), by intraperitoneal injection to pregnant dams (doxycycline: E13.5>E15.5; verteporfin: daily E13.5>E18.5; **Figure 6a**). Morphological analysis at P0 confirmed that verteporfin treatment indeed attenuated the Pik3ca-related gyrification severity and completely rescued ventriculomegaly in 100% of the mutant brains, with little effect on control CA1 ventricular-subventricular zone morphology (**Figure 6b-g, Figure 6 – figure supplement 1a-h,j**).

Using laser-capture method, we micro-dissected ventricular regions of the hippocampi from verteporfin treated and untreated mice, isolated RNA and performed RNA sequencing. Principal component analysis of the global transcriptional profiles of laser micro-dissected P0 CA1 ventricular-subventricular zone tissue (**Figure 6e-i**)

confirmed that the untreated *Pik3ca* mutant samples (both gyrus and sulcus) were clearly distinct from the control samples. Verteporfin treatment had minimal effect on gene expression of control tissue but shifted the mutant gene expression profiles towards controls. Specifically, verteporfin treatment caused the mutant sulcus samples to cluster together with control samples, while treated mutant gyrus samples showed evidence of partial normalization. As expected, *Pik3ca* expression was higher in mutant samples, and suppressed post-verteporfin treatment, reflecting the complex feedback signaling in the PI3K pathway (Carracedo and Pandolfi, 2008). Gene set enrichment analysis confirmed that PI3K and Hippo-Yap signaling pathways were significantly differentially regulated in untreated mutants compared to controls, as expected (**Figure 6 – figure supplement 2a-d, Figure 6 – Source Data 1 and 2**). Verteporfin treatment brought both PI3K and Hippo-Yap gene expression in mutants close to control levels, especially at the sulci. Notably, there was a considerable overlap in the gyral and sulcal gene expression profiles of our *Pik3ca*^{H1047R} mutant mice and those mapped from ferret (de Juan Romero et al., 2015) – a naturally gyrencephalic mammal (**Figure 6 – figure supplement 3a,b**). These suggest that our activating *Pik3ca* mutant gyrification model has significant physiological relevance to at least this naturally gyrencephalic species.

Immunohistochemical analyses of P0 verteporfin-treated mutants revealed normalized apical cell polarity in both the regions of attenuated sulci and gyri, with elimination of ectopic nYap⁺ cells and rescue of contiguous apical ZO1 and cYap localization (**Figure 7b,c,h-i',n-o'**). Verteporfin normalized both nYap⁺ and Six3⁺ cell number and distribution in P0 mutant gyri and sulci (**Figure 6 – figure supplement 1k,l; Figure 7h',n',t,u**). The 5-day acute verteporfin treatment of mutant mice resulted

308 in streamlined Vimentin⁺/Nestin⁺ radial glia, denser CA1 PL cell packing and reduction in
309 the Tbr2⁺ basal progenitor pool to almost control levels (**Figure 7d-g,j-m',p-s',v**).
310 Restoration of P0 mutant ventricular cell polarity was readily apparent with β -Catenin
311 and N-Cadherin expression, which also highlighted the close apposition of the
312 neocortical and hippocampal ependymal surfaces (**Figure 7 – figure supplement 1a-**
313 **i'**). The effect of verteporfin on tissue architecture was identifiable even early, as studied
314 in E16.5 *Pik3ca*^{H1047R} mutants and control littermates (**Figure 7 – figure supplement**
315 **2a-c**). Compared to the untreated mutants, E16.5 verteporfin-treated mutants
316 (verteporfin: E13.5>E16.5) demonstrated increased alignment of junctional proteins,
317 normalized progenitor pool numbers and reduced occurrence of unzipped apical
318 membranes (**Figure 7 – figure supplement 2d-g'**). TUNEL assay showed no
319 significant difference in apoptotic cell number between E16.5 control and mutant CA1,
320 both in untreated and in verteporfin-treated conditions, indicating that cell death is not
321 an important factor influencing the mutant phenotypes (**Figure 7 – figure supplement**
322 **2h**). The effect of PI3K-Yap interactions on cell adhesion and proliferation is
323 summarized in **Figure 8a-c**.

DISCUSSION

Cortical gyrification or its absence is an essential feature of mammalian brain evolution but the mechanisms driving cortical folding, particularly its initiation, are poorly understood (Borrell, 2018). Using our activating *Pik3ca* mutant mouse model of human cortical malformations (Roy et al., 2015), we have established that regulated cell adhesion and proliferation via PI3K-Yap signaling at the apical edge of the embryonic ventricular zone is critical to maintain the lissencephalic nature of mouse brain and prevent developmental hydrocephalus. Overactivation of PI3K signaling in neural progenitors during a critical embryonic period (E13.5-E15.5) led to “true” gyrification (Borrell, 2018) of the mutant mouse neocortex and hippocampus, with the stereotypic characteristics of folded pial surface and neuronal plate/white matter of differential thickness, with predominantly smooth apical ventricular surfaces. This transient PI3K activation was also sufficient to initiate a stereotypic neurogenic sequence similar to that seen in naturally gyrencephalic mammals, such as ferrets (Reillo and Borrell, 2012, de Juan Romero et al., 2015). This sequence includes differential proliferation of primary and secondary (IPs, bRGs) progenitors, cell differentiation and migration, and an altered radial glial scaffold. PI3K overactivation did not disrupt gross hippocampal patterning but did cause subtle disruptions in cell adhesion at the apical edge. Adhesion abnormalities were concurrently associated with aberrant focal cytoplasmic-to-nuclear translocation of Yap protein, which predicted the stereotypical positioning of the gyral foci. Hydrocephalus in this model was also associated with the disruption of PI3K-dependent apical adhesion in the same progenitors, but across a broader embryonic time-period. Both the gyrification and hydrocephalic phenotypes were 100% penetrant

in the mutants and were attenuated by embryonic treatment with verteporfin, a nYap inhibitor, which normalized apical junctions and proliferation along the mutant ventricular linings. Our data provide new insights regarding the mechanisms that initiate gyrification in mammals, and apical adhesion alterations in human PI3K-related disorders that contribute to the broad range of neuropathology including impaired brain folds and ventriculomegaly.

***Pik3ca* mis-regulation altered cell adhesion at the apical edge of cortical ventricular zone**

Brief activation of the *Pik3ca*^{H1047R} mutation resulted in focal disruption of adhesion, as observed in the loose “zippering” of the ventricular linings, subtle initial changes and then gaps in the expression of adhesion molecules β -Catenin, N-Cadherin and ZO-1, especially in the prospective sulci. This in turn impinged on the development of neuronal and ependymal progenitors. Interestingly, the developing ferret brain also demonstrates differential regional variation in cell adhesion and junctional proteins at the prospective gyrus and sulcus (de Juan Romero et al., 2015). Genes that were differentially expressed between the gyrus and sulcus in ferret were enriched in our *Pik3ca*^{H1047R} mutant, with considerable overlap in cell adhesion-related genes. This demonstrates potential physiological relevance of our model to naturally gyrencephalic mammals, although additional experiments may be required.

The ventricular surface of the developing brain is formed by tangential assembly of the apical end-feet of progenitor cells, enriched in adherens junction molecules, ZO-1 and Cadherins (Nagasaka et al., 2016). Loss-of-function mutations in the cell adhesion

machinery, such as *fyn*, *Cdh2* (N-Cadherin) cause dysplastic hippocampal morphology (Grant et al., 1992, Kadowaki et al., 2007). Recently, adhesion-ECM molecules, like E-cadherin, connexins, FLRT1/3, filamin, have been identified, that influence the balance in adhesion-repulsion forces between migrating neurons to cause interspersed cell clustering with differential migration speed, eventually establishing the cortical sulci (Borrell, 2018, Llinares-Benadero and Borrell, 2019). It is interesting to note that all these molecules have well-established functional interactions with the PI3K pathway (Gout et al., 1992, Tran et al., 2002, Najib et al., 2012, Huang et al., 2015, Martinez et al., 2015).

Perhaps the closest published model to our new *Pik3ca* mouse model is the *D6-cre;Cdh2* conditional knockout (Kadowaki et al., 2007), which exhibited folding in the CA1 PL. However, the loss of N-Cadherin in early differentiating neurons induced complete disruption of adherens junctions, resulting in abnormalities of internal cortical structures, dysplastic radial glial architecture and cellular lamination, and blurring of the lateral neocortex–hippocampus delineation. Such severe developmental defects are neither observed in normal gyrencephalic mammals nor in our mutant mouse model. Rather in our model, *Pik3ca* activation caused much more subtle disruption of apical junctions, resulting in cortical folding with broadly normal lamination, as observed in naturally gyrencephalic animals.

The PI3K enzyme is composed of p110 (encoded by *Pik3ca*) and p85 subunits (Geering et al., 2007). Previous studies have demonstrated that *Pik3ca*^{H1047R} allele remains tightly dependent on p85 regulation (Geering et al., 2007, Zhao and Vogt, 2008, Roy et al., 2015). Hence, although the *Pik3ca*^{H1047R} allele is a strongly activating

mutation with higher kinase activity (Gymnopoulos et al., 2007), it is functionally not an overexpression allele to cause massive pathway induction. Taken together, our data indicate that exquisite PI3K-dependent regulation of apical cell adhesion is essential for normal mouse brain development and suggests that subtle regional changes in other mammals may initiate natural gyrification. This hypothesis should be readily testable but is beyond the scope of our current study.

PI3K-dependent modulation of Yap protein function is central to initiation of gyrification

Focal loss of apical integrity and over-proliferation of neural progenitors in our *Pik3ca* model highly correlated with focal areas of translocation of Yap protein from the apical cytoplasmic edge to nuclei at the ventricular lining. Yap is a central regulator of the Hippo pathway, with both nuclear and cytoplasmic functions (Gumbiner and Kim, 2014, Park et al., 2016, Park et al., 2018). The Hippo-Yap pathway is known to mediate mechanical signals, cellular stress, polarity and adhesion cues that are integrated through multiple upstream regulators (Hansen et al., 2015). Phosphorylated Yap is sequestered in the cytoplasm by adherens junction proteins. In turn, cYap, expressed in the early developing ependyma, has been shown to critically maintain cell-cell adhesion at the ventricular edge of ventral aqueduct (Park et al., 2016). When dephosphorylated, Yap translocates to the nucleus, where it binds to TEAD transcriptional co-regulators to modulate gene expression (Hansen et al., 2015, Park et al., 2018). In this context, nYap was recently shown to be sufficient to drive cortical progenitor proliferation (Lavado et al., 2018).

We hypothesized that PI3K regulation of Yap subcellular distribution was central to the gyrification phenotype in our *Pik3ca*^{H1047R} mutant mouse model. *In vitro*, PI3K-PDK1 pathway activation promotes nuclear translocation of Yap, thus disrupting contact inhibition (Fan et al., 2013). Verteporfin, a nYap antagonist, disintegrates the Yap-TEAD nuclear complex, facilitating sequestration of Yap to the cytoplasm (report, 2000, Schmidt-Erfurth and Hasan, 2000, Liu-Chittenden et al., 2012, Fan et al., 2013, Brodowska et al., 2014, Gumbiner and Kim, 2014). Treatment of *Pik3ca*^{H1047R} mutants with verteporfin restored the apical cYAP distribution in progenitors, rescued the integrity of the ventricular surface, reduced the enhanced progenitor proliferation and subsequently attenuated the gyrification of the *Pik3ca*^{H1047R} mutant mice. To our knowledge, this is the first study where verteporfin was introduced intraperitoneally into the pregnant mice to successfully suppress nYap function in embryos across the placental barrier.

We did not fully rescue the gyrification phenotype, likely because PI3K signaling has a multitude of downstream outputs in addition to Yap regulation. Although we cannot rule out potential off-target effects of verteporfin, our data provide strong evidence that PI3K pathway modulation of the cYap pool during the brief embryonic critical period is essential to maintain the lissencephalic mouse brain. We speculate that subtle changes in local apical adhesion properties of early progenitors, associated with focal changes in Yap subcellular distribution and subsequently in the basal progenitor population, is one of the initiating mechanisms of gyrification in higher mammals. This may also be linked to changes in centrosome and microtubule organization in apical progenitors (Camargo Ortega et al., 2019). Further, a recent study has demonstrated

that YAP maintains basal progenitor population in the developing ferret and human neocortex (Kostic et al., 2019). Similar to our current findings, this study also showed that YAP regulation by verteporfin in *ex vivo* embryonic ferret and fetal human neocortical free-floating tissue culture systems leads to reduction in basal progenitor number (Kostic et al., 2019). However, further analysis of all these parameters in ferrets (Borrell, 2018) and other model systems is required.

Cortical folding patterns in naturally gyrencephalic species are highly stereotypic, although there is considerable inter-individual variation (Ronan and Fletcher, 2015, Borrell, 2018). Importantly, the gyrification pattern induced in *GFAP-cre;Pik3ca^{H1047R}* mutants was non-random, with 100% penetrance, and was highly cre-dependent (Roy et al., 2015, D'Gama et al., 2017). We do not currently understand why gyri form in stereotypical positions in *Pik3ca^{H1047R}* mutant mice or indeed, in any normal gyrencephalic mammal. We hypothesize that cell-cell adhesion is less constrained in susceptible focal positions compared to adjacent regions during the critical periods of development. These coordinates may be defined by genetically encoded signaling gradients or may simply be a result of regional variations in mechanical force (Ronan and Fletcher, 2015, Borrell, 2018). Developing cortical tissue from naturally gyrencephalic mammals is of limited availability, making extensive experimentation difficult. The highly regulatable stereotypical and fully penetrant gyrification phenotype of *Pik3ca^{H1047R}* mutant mice provides a new, highly tractable alternative model to unravel the positional constraints giving rise to brain folds.

Yap-dependent apical cell adhesion mediates normal ependymal development and its disruption likely underlies multiple types of pediatric hydrocephalus amenable to small molecule therapy

In addition to gyrification, embryonic induction of *Pik3ca*^{H1047R} allele in mouse neural progenitors also caused ventriculomegaly which progressed postnatally to hydrocephalus. Hydrocephalus is a common feature of human PI3K-related brain overgrowth syndromes (Mirzaa et al., 2012, Tully and Dobyns, 2014, Guerra et al., 2015, Khan et al., 2015). We determined that PI3K-dependent ventriculomegaly had long embryonic critical period, ending at E17.5, compared to the short gyrification critical period (E13.5-E15.5). Embryonic verteporfin-dependent nYap inhibition also rescued ventriculomegaly, with minimal effect on control littermates. We conclude that disrupted apical cell adhesion and aberrant nYap localization were central to this phenotype as well as gyrification.

Hydrocephalus is often associated with a disrupted ependyma, although in many cases it is unclear if this is because of abnormal ependymal development or ependymal damage at a later stage (Jimenez et al., 2014). The ependyma is a continuous single layer of neuroepithelial multi-ciliated cells lining the lateral ventricles. Ependymal cells differentiate from apical progenitors and mature during late embryogenesis and early postnatal mouse development, when most definitive ependymal markers, including FoxJ1 and other markers of multi-ciliated cells, are expressed (Schmidt-Erfurth and Hasan, 2000, Lavado and Oliver, 2011). Little is understood regarding the primary molecular control of ependymal specification. In our mutant mouse model, the normally uniform layer of Vimentin⁺/Yap⁺ developing ependymal cells was disrupted at mid-

embryonic stages. Further, cells with ependymal fate (Yap⁺) were intermingled with Tbr2⁺ progenitors and young Ctip2⁺ neurons at the mutant gyral edge, indicating abnormal neural-to-ependymal transition. This phenotype and the subsequent hydrocephalus were reversed with verteporfin treatment, although the drug-treated ependyma was not entirely normal. These data clearly demonstrate that early Yap-dependent apical adhesion is required for normal ependymal development in forebrain during embryonic pre-ciliogenesis stages – a developmental time much earlier than previously established.

Interestingly, human post-mortem studies and *in vitro* model studies have shown disruption of cell adhesion and apical junctions in post-hemorrhagic hydrocephalus, a common form of hydrocephalus in premature infants, currently with few treatment options (Morales et al., 2012, Jimenez et al., 2014, Guerra et al., 2015). In mice, embryonic intraventricular administration of blood-derived lysophosphatidic acid (LPA), is sufficient to cause disrupted ependymal cell adhesion and neonatal hydrocephalus in mice (Yung et al., 2015). More recently, Park *et al.* (2016) showed that depletion of cYAP, by either genetic deletion or LPA treatment, also resulted in perinatal hydrocephalus due to impaired ependymal development and aqueduct blockage (Park et al., 2016). Taken together with our data, we posit that altered periventricular cell adhesion caused by dysregulated Hippo-Yap signaling is a common convergent mechanism for both developmental and post hemorrhagic hydrocephalus. Fine regulation of the Hippo-Yap pathway may represent a new therapeutic approach for pediatric hydrocephalus patients, especially since verteporfin effectively crosses the placenta and has minimal effect on normal brain development as demonstrated by our

morphological and RNA-seq analyses. This implication is worthy of further detailed preclinical analysis.

In summary, building upon our original study of mouse models of human *PIK3CA*-related brain malformations (Roy et al., 2015), we demonstrate intimate PI3K-dependent developmental and molecular links between cortical neurogenesis and ependymal development at the apical edge of the embryonic ventricular zone. Disruption of apical surface integrity in the forebrain, via enhanced embryonic PI3K-Yap signaling, alters neurogenesis and can initiate *bona fide* gyrification in mice. This process mimics the canonical neurogenic sequence observed in naturally gyrencephalic mammals. Concurrently, abnormal apical PI3K-Yap interaction disrupts ependymal development in forebrain, prior to ciliogenesis, leading to hydrocephalus. Our data readily explain the coincidence of impaired neurogenesis, gyrification and hydrocephalus, observed often in patients with cortical dysplasia and in our *Pik3ca* mouse model (Keppler-Noreuil et al., 2014, Jansen et al., 2015, Roy et al., 2015, Parrini et al., 2016, Furey et al., 2018). The results also provide support for nuclear Yap protein as a potential new therapeutic target for these clinically important disorders.

524 Key Resources Table

| Reagent type (species) or resource | Designation | Source or reference | Identifiers | Additional information |
|---|---|--|---|---|
| Genetic reagent (<i>Mus musculus</i>) | <i>GFAP-cre</i> | gift (JJ Zhao); PMID: 11668683 | (IMSR Cat# JAX:004600 , RRID:IMSR_JAX:004600) | gifted by Dr. Jean J Zhao (Dana Farber Cancer Inst., Boston, USA) |
| Genetic reagent (<i>Mus musculus</i>) | <i>Pik3ca</i> ^{H1047R} | gift (JJ Zhao); PMID: 21822287 | MGI: 5526971 | gifted by Dr. Jean J Zhao (Dana Farber Cancer Inst., Boston, USA) |
| Genetic reagent (<i>Mus musculus</i>) | <i>Ai14/+; Ai14</i> | Jax labs (stock #007914), PMID: 20023653 | (IMSR Cat# JAX:007914, RRID:IMSR_JAX:007914) | PMID: 20023653 |
| Genetic reagent (<i>Mus musculus</i>) | <i>Rosa26-rtTA; Rosa</i> | PMID: 15784609 | (IMSR Cat# JAX:005670 , RRID:IMSR_JAX:005670) | gifted by Dr. Jean J Zhao (Dana Farber Cancer Inst., Boston, USA) |
| Antibody | Anti-BrdU antibody [BU1/75 (ICR1)] | Abcam | (Abcam Cat# ab6326 , RRID:AB_305426) | IHC (1:100) |
| Antibody | Anti-BrdU-Fluorescein antibody Formalin grade | Roche | (Roche Cat# 11202693001 , RRID:AB_514484) | IHC (1:100) |
| Antibody | Rabbit anti Calbindin D-28k | Swant | (Swant Cat# CB38 , RRID:AB_2721225) | IHC (1:1500) |
| Antibody | Anti-Ctip2 antibody [25B6] - ChIP Grade | Abcam | Abcam Cat# ab18465 , RRID:AB_2064130) | IHC (1:250) |
| Antibody | Rabbit GFAP antibody | Dako (now Agilent) | (Agilent Cat# Z0334 , RRID:AB_10013382) | IHC (1:2500) |
| Antibody | Anti-Neural Cell Adhesion Molecule L1 Antibody, clone 324 | Millipore | (Millipore Cat# MAB5272 , RRID:AB_2133200) | IHC (1:200) |
| Antibody | Rabbit Anti-Laminin | Sigma | (Sigma-Aldrich Cat# L9393 , RRID:AB_477163) | IHC (1:25) |
| Antibody | Purified Mouse Anti-N-Cadherin | BD Biosciences | (BD Biosciences Cat# 610921 , RRID:AB_398236) | IHC (1:150) |
| Antibody | Mouse Anti-Nestin Antibody, clone rat-401 | Millipore | (Millipore Cat# MAB353 , | IHC (1:200) |

| | | | | |
|----------|--|--------------------------|--|---|
| | | | RRID:AB_94911) | |
| Antibody | Rabbit Purified anti-Pax-6 Antibody | Biolegend | (BioLegend Cat# 901301, RRID:AB_2565003) | IHC (1:300) |
| Antibody | Mouse anti-Pax6 antibody | DSHB | N/A | IHC (1:300; deposited in DSHB by Kawakami A.) |
| Antibody | Phospho-Histone H3 (Ser10) (6G3) Mouse mAb | Cell Signaling | (Cell Signaling Technology Cat# 9706, RRID:AB_331748) | IHC (1:200) |
| Antibody | Anti-Reelin Antibody, a.a. 164-496 mouse reelin, clone G10 | Millipore | (Millipore Cat# MAB5364, RRID:AB_2179313) | IHC (1:1200) |
| Antibody | Anti-SATB2 antibody [SATBA4B10] - C-terminal | Abcam | (Abcam Cat# ab51502, RRID:AB_882455) | IHC (1:400) |
| Antibody | Rabbit anti-Six3 polyclonal antibody; | Rockland Antibodies | (Rockland Cat# 600-401-A26S, RRID:AB_11181864) | IHC (1:200) |
| Antibody | Rabbit anti-Sox2 antibody | Thermo Fisher Scientific | (Thermo Fisher Scientific Cat# PA1-094, RRID:AB_2539862) | IHC (1:400) |
| Antibody | Rabbit anti-Tbr1 antibody | Millipore | (Millipore Cat# AB10554, RRID:AB_10806888) | IHC (1:400) |
| Antibody | EOMES Monoclonal Antibody (Dan11mag) Tbr2 antibody | eBioscience | (Thermo Fisher Scientific Cat# 14-4875-82, RRID:AB_11042577) | IHC (1:200) |
| Antibody | Anti-Vimentin antibody [EPR3776] - Cytoskeleton Marker | Abcam | (Abcam Cat# ab92547, RRID:AB_10562134) | IHC (1:200) |
| Antibody | YAP (D8H1X) XP® Rabbit mAb | Cell Signaling | (Cell Signaling Technology Cat# 14074, RRID:AB_2650491) | IHC (1:100) |
| Antibody | ZO-1 Monoclonal Antibody (ZO1-1A12), Alexa Fluor 488 | Thermo Fisher Scientific | (Thermo Fisher Scientific Cat# 339188, RRID:AB_2532187) | IHC (1:500) |
| Antibody | Purified Mouse Anti-β-Catenin Clone 14 | BD Biosciences | (BD Biosciences Cat# 610154, RRID:AB_397555) | IHC (1:200) |
| Antibody | Rabbit β-Catenin antibody | Abcam | (Abcam Cat# ab2365, RRID:AB_303014) | IHC (1:100) |
| Antibody | Goat anti-Rat IgG (H+L) Cross-Adsorbed Secondary Antibody, Alexa Fluor 647 | Thermo Fisher Scientific | (Thermo Fisher Scientific Cat# A-21247, RRID:AB_141778) | IHC (1:400) |

| | | | | |
|-------------------------|--|-----------------------------|---|-------------|
| Antibody | Goat anti-Mouse IgG (H+L) Highly Cross-Adsorbed Secondary Antibody, Alexa Fluor 488 | Thermo Fisher Scientific | (Thermo Fisher Scientific Cat# A-11029, RRID:AB_2534088) | IHC (1:400) |
| Antibody | Goat anti-Rabbit IgG (H+L) Highly Cross-Adsorbed Secondary Antibody, Alexa Fluor 568 | Thermo Fisher Scientific | (Thermo Fisher Scientific Cat# A-11036, RRID:AB_10563566) | IHC (1:400) |
| other | DAPI stain | Molecular Probes | (Thermo Fisher Scientific Cat# D1306, RRID:AB_2629482) | 1:10000 |
| Commercial assay or kit | ApopTag Plus Fluorescein In situ Apoptosis Detection Kit | Chemicon/ Millipore | Cat# S7111 | |
| Commercial assay or kit | SMART-Seq v4 Ultra Low Input RNA Kit | Takara | Cat# 634889 | |
| Commercial assay or kit | Nextera XT kit | Illumina | Cat# FC-131-1024 | |
| Commercial assay or kit | KAPA qPCR complete kit | Biorad | KK4844 Complete kit 500x20ul reactions | |
| Commercial assay or kit | RNeasy Micro Kit | Qiagen | Cat# 74004 | |
| Commercial assay or kit | Bioanalyzer 6000 Pico Kit | Agilent | Cat# 5067-1513 | |
| chemical compound, drug | Verteporfin | US Pharmacopeial Convention | Cat# 1711461 | |
| chemical compound, drug | BrdU Labeling Reagent | Life Technologies | Cat# 000103 | |
| chemical compound, drug | Doxycycline (doxycycline hyclate) | Sigma | Cat# D9891-25G | |
| software, algorithm | BioViz3D version 3.1 | BioViz3D | BioViz3D, RRID:SCR_017162 | |
| software, algorithm | salmon aligner v0.11.3 for R | PMID: 28263959 | | |
| software, algorithm | Bioconductor tximport package, v1.8.0 for R | PMID: 26925227 | | |
| software, algorithm | Bioconductor edgeR package v3.22.3 | PMID: 19910308 | (Bioconductor, RRID:SCR_006442) | |
| software, algorithm | glmTreat function in edgeR | PMID: 19176553 | | |
| software, algorithm | Bioconductor GEOquery v2.48.0 | PMID: 17496320 | (GEOquery, RRID:SCR_000146) | |

| | | | | |
|------------------------|----------------------------------|-------------------|--|--|
| software, algorithm | limma packages, v3.36.2 for R | PMID: 25605792 | | |
|------------------------|----------------------------------|-------------------|--|--|

525

526 **Mice**

527 The following mouse lines were used: human glial fibrillary acidic protein (*hGFAP*)-*cre*
528 (Jackson Labs, IMSR Cat# JAX:004600, RRID:IMSR_JAX:004600) (Zhuo et al., 2001),
529 mentioned as *GFAP-cre* in this study; *Pik3ca*^{H1047R} transgenic (human *Pik3ca*^{H1047R}
530 transgene expression is under the control of a tetracycline-inducible promoter (TetO)),
531 *Rosa26-rtTA* line (Jackson Labs, Stock #005670) (Belteki et al., 2005), Ai-14 (Jackson
532 Labs, Stock #007914) (Madisen et al., 2010).

533 All lines were maintained on a mixed genetic background, comprising of FVB, 129 and
534 CD1 strains. All mice were housed in Optimice cages with aspen bedding at the Seattle
535 Children's Research Institute's specific pathogen-free (SPF) vivarium facility. Noon of
536 the day of vaginal plug was designated as embryonic day 0.5 (E0.5). The day of birth
537 was designated as postnatal day 0 (P0). The *Pik3ca*^{H1047R} and *Rosa26-rtTA* lines were
538 intercrossed and female mice positive for both these alleles were crossed with *GFAP-*
539 *cre;RosartTA; Pik3ca*^{H1047R} males. Embryos or pups of both sexes, genotyped positive
540 for all three genes, namely *cre*, *Rosa*, *Pik3ca*^{H1047R}, were used in this study. The *GFAP-*
541 *cre* driver gets activated in neural progenitors only at ~E13 (Zhuo et al., 2001, Roy et
542 al., 2015). The activating *H1047R* mutation in the PI3K catalytic subunit (*Pik3ca*)
543 increases the level and duration of response to extracellular ligands, its stability being
544 completely dependent on the unaltered level of the p85 regulatory subunit (Roy et al.,
545 2015). To ensure that *cre* and *Pik3ca*^{H1047R} mutant transgene expression was
546 correlated, plugged females were treated with doxycycline (Sigma; 2mg/ml) from E0.5

or as mentioned in the text, available *ad libitum* in drinking water. For the neonatal induction experiment, the pups were treated with doxycycline from P1. The *GFAP-cre;RosartTA;Pik3ca^{H1047R}* mutant is mentioned as *Pik3ca^{H1047R}* mutant in the text. Mouse genotyping by PCR was done using separate sets of primers for the *Cre* coding region, and the *Pik3ca^{H1047R}*, *Rosa+/-*, and *Ai14/+* alleles, as previously described (Roy et al., 2015). All mouse procedures were approved and conducted in accordance with the guidelines laid down by the Institutional Animal Care and Use Committees (IACUC) of Seattle Children's Research Institute, Seattle, WA, USA.

Sample preparation and histochemical procedures

Embryos and postnatal pups were harvested in phosphate buffer saline (PBS); brains fixed in 4% paraformaldehyde (PFA) for 4 hours, equilibrated in 30% (wt/vol) sucrose made in PBS, and sectioned at 25µm on a freezing microtome. Sections were then processed for Nissl or immunohistochemical staining. No data were excluded from our analysis and no randomization was used. Tissue collection was not performed blind since the mice were subjected to genotyping and drug administration. However, the data analysis was performed blinded by at least 2 individuals.

Immunohistochemistry (IHC): Sections were washed thrice in PBS, boiled in 10mM Sodium citrate solution for antigen retrieval, blocked in 5% serum in PBS with 0.1% Triton X-100 and then incubated overnight at 4°C with primary antibodies. The next day, sections were washed thrice in PBS, incubated with appropriate species-specific secondary antibodies conjugated with Alexa 488, 568 or 647 fluorophores (Invitrogen) for 2hr at room temperature and then counterstained with DAPI (4',6-Diamidino-2-

570 Phenylindole, Dihydrochloride; Invitrogen; D1306) to visualize nuclei. Sections were
571 cover-slipped using Fluorogel (Electron Microscopy Sciences, EMS #17985) mounting
572 medium. Immuno-stained sections were imaged in Zeiss LSM 710 Imager Z2 laser
573 scanning confocal microscope using Zen 2009 software and in Olympus VS-120 slide-
574 scanner microscope using Olympus VS-Desktop 2.9 software, and later processed in
575 ImageJ 1.51j8 and ImageJ2 (NIH, Bethesda, Maryland, USA) and Olympus VS-Olyvia
576 2.9 software programs respectively. Each antibody was validated for mouse and
577 application (IF, IHC) by the correspondent manufacturer, and is publicly available on its
578 website with indicated catalogue numbers. This was also validated by us in our
579 experiments, replicating published/expected expression in control tissue. Primary
580 antibodies used: rat anti-BrdU (Abcam), mouse anti-BrdU (Roche), rabbit anti-Calbindin
581 (Swant), rat anti-Ctip2 (Abcam), rabbit anti-GFAP (Dako), rat anti-L1 (Millipore), rabbit
582 anti-Laminin (Sigma), mouse anti-N-Cadherin (BD Biosciences), mouse anti-Nestin
583 (Millipore), rabbit anti-Pax6 (Biolegend), mouse anti-Pax6 (DSHB), mouse anti-
584 phospho-Histone H3 (Cell Signaling), mouse anti-Reelin (Millipore), mouse anti-Satb2
585 (Abcam), rabbit anti-Six3 (Rockland Antibodies), rabbit anti-Sox2 (Thermofisher), rabbit
586 anti-Tbr1 (Millipore), rat anti-Tbr2 (eBioscience), rabbit anti-Vimentin (Abcam), rabbit
587 anti-Yap (Cell Signaling), mouse anti-ZO-1 (), mouse anti- β -Catenin (BD Biosciences),
588 rabbit anti- β -Catenin (Abcam). Immuno-histochemistry replication consisted of
589 performing the same experiment with biologically independent samples from the same
590 group (control or mutant +/- drug). All attempts for replication were successful. No
591 outliers were encountered. Each antibody was validated for mouse and application
592 (IHC) by the correspondent manufacturer and is publicly available on its website with

indicated catalogue numbers. This was also validated by us in our experiments, replicating published/expected expression in control tissue.

Nissl staining: Sections were stained in 0.1% cresyl violet solution (Cresyl violet, Sigma Cat# C5042) for 10min, rinsed quickly in distilled water, dehydrated in 95% ethanol, and left in xylene before being cover-slipped with Permount (Thermo Fischer Scientific, SP15-500). Brightfield images were taken in the Olympus VS-120 slide-scanner with Hamamatsu digital camera C11440 and processed using the Olympus VS-Olyvia 2.9 software.

BrdU Incorporation Experiments

Bromodeoxyuridine (BrdU; Life Technologies) was administered intraperitoneally (100 µg/g of body weight) to pregnant dams at E14.5/16.5 for 1 hour, at E15.5 for 1 day and at E16.5 for proliferation assays, cell cycle exit and birth-dating experiments respectively. Labeling index and quit fraction were calculated as previously described (Roy et al., 2015).

3-D modeling and video

3-D models of P3 (dox E0.5 to P3) control and *GFAP-cre;Pik3ca*^{H1047R} mutant hippocampus were developed using the software BioViz3D version 3.1. About 16 serial coronal sections (30 microns each) of Nissl-stained P3 control and mutant hemi-sections of forebrain were imaged and arranged in the rostro-caudal order. Contours were drawn in each section, based on morphology for the entire medial forebrain tissue

and the hippocampus. The 3-D reconstruction was created using these contours from each section. The control and mutant models were marked purple and red respectively. The medial tissue for both the control and mutant were marked in a lighter shade of the afore mentioned color, to be distinguished from the darker PL. The movie was made using the movie maker software within BioViz3D and edited with VLC media player.

Verteporfin treatment

Verteporfin (20mg/ml stock solution made in 100% mineral oil) was administered intraperitoneally at the dose of 1 μ l/g of body weight, one injection per day into timed pregnant dams from E13.5 to E18.5, and the neonatal pups were harvested at P0. The number of mouse brains analyzed was 7/genotype (+/- verteporfin), obtained across 5 P0 litters. 100% of the mutant brains demonstrated attenuation of the gyrfication and hydrocephalus phenotypes post-verteporfin treatment. For the shorter experiment, same dose of verteporfin was administered to pregnant dams from E13.5 to E16.5 and embryos were harvested at E16.5 (n=4 brains/genotype/condition).

TUNEL staining

TUNEL staining was processed on E16.5 control and mutant sections (+/- Verteporfin) using **ApopTag Plus Fluorescein In situ Apoptosis Detection Kit**.

Laser capture micro-dissection (LCM)

Whole forebrains were dissected from P0 (dox E13.5>E15.5) control and mutant mice (+/- verteporfin). These intact forebrains were then embedded in OCT, frozen at -80°C, and cryo-sectioned at 16µm in the coronal plane onto PEN Membrane Glass Slides (Leica Microsystems, USA). The sections were stained with Cresyl Violet (Nissl stain). LCM was performed using the Leica LMD-6000 Laser Microdissection system to capture tissue containing the hippocampal CA1 ventricular lining of control brains and mutant hippocampal gyri and sulci, from each of the 12-14 sections mounted per slide into collection tubes. Total RNA was isolated from LCM-enriched samples pooled across ~6 slides per genotype using the Qiagen RNeasy Micro Kit and RNA quality was assessed using the Agilent Bioanalyzer 6000 Pico Kit [RNA Integrity Number (RIN) = 7.68 ± 0.26 (mean \pm s.d.)].

RNA sequencing and analysis

Three sequencing libraries were prepared from each RNA sample using 5 ng total RNA in the SMART-Seq v4 Ultra Low Input RNA Kit (Takara), according to the manufacturer's protocol. The cDNA was fragmented and tagged with sequencing adapters using Nextera XT kit (Illumina). The transcripts were quantified with the KAPA qPCR complete kit (BioRad) for Illumina platforms. RNA libraries were sequenced on Illumina HiSeq 4000 platform. Library preparation and sequencing were performed by the Northwest Clinical Genomics Laboratory at the University of Washington. We aligned reads to the mm10 transcriptome using the salmon aligner v0.11.3,(Patro et al., 2017) and then imported into R and summarized at the gene level using the Bioconductor tximport package, v1.8.0 (Soneson et al., 2015). We then filtered out any

genes with consistently low counts (retaining those genes with >10 counts in at least 3 samples). After filtering, 19,339/35,728 (54%) genes remained. Differential gene expression was performed using the Bioconductor edgeR package v3.22.3 (Robinson et al., 2010), implemented in the R programming language. We fit the model and then made comparisons using quasi-likelihood F-tests. We incorporated a log fold change $>\pm 0.263$ (representing a 20% change in expression) as part of the comparison, using the glmTreat function in edgeR (McCarthy and Smyth, 2009), and selected genes with a false discovery rate (FDR) <0.05 . We then performed a set of self-contained gene set tests based on the PI3K pathway ([GO:0043491](#)), YAP pathway ([GO:0035329](#)), and the genes that are differentially expressed between the developing gyrus and sulcus in ferret (de Juan Romero et al., 2015). To generate the gene set based on ferret brain, we downloaded and processed data from the Gene Expression Omnibus ([GSE60687](#)), using the Bioconductor GEOquery v2.48.0 and limma packages, v3.36.2 (Davis and Meltzer, 2007, Ritchie et al., 2015), identifying 362 genes with $FDR < 0.1$. We used NCBI BLAST+ to align probe sequences to the RefSeq database, then matched gene symbols to our mouse RNA-seq dataset, resulting in 168 matching genes. We generated barcode plots to help visualize results from the gene set tests using functions in the limma package. Bar graph was made in Microsoft Excel using log transformed counts, after normalizing for library size (log counts/million counts). Venn diagram was made using the online application <http://bioinformatics.psb.ugent.be/webtools/Venn/>.

Quantitative Analysis

683 Number of mice is consistent with previous experiments completed and published by us
684 and other investigators and based on power analyses. For histology and length
685 measurement experiments, we performed power analyses in R using the pwr package.
686 We used preliminary data to estimate sample variance and calculated an effect size of
687 1.8 between groups. We then used this effect size of 1.8 to estimate that a sample size
688 of 5 animals per group will be required to have 80% power to detect significant
689 differences ($p=0.05$) between groups. Based on this, we considered group size of 5-8
690 mice/genotype for each experiment to be sufficient, unless otherwise specified; extra
691 mice/cells were considered for possible technical issues. For quantitative analysis of
692 embryos, data was collected from comparable sections of each genotype/condition
693 (from 2 or more independent litters) at each developmental stage. All measurements
694 were made using ImageJ and ImageJ2 software programs (NIH, Bethesda, Maryland,
695 USA). Medial tissue length was measured in the lateral ventricular lining from the dorso-
696 medial cortical notch to the fimbrial tip (Roy et al., 2015); the data was normalized to the
697 control value ($n=8$ /genotype). P3 critical period CA1 length was measured along the
698 mid-thickness of the PL of each mutant type; data was normalized to the P3 CA1 length
699 (induced E0.5>P0). Cell counts from E14.5, E16.5 and P0/P3 brains were obtained from
700 the middle part of the CA1 dorso-ventral extent. To avoid counting discrepancies related
701 to decreased cell density in E16.5 *Pik3ca* mutant (Roy et al., 2015), all E16.5 cell
702 counts were done by dividing each cell type by the total number of DAPI⁺ cells present
703 within the fixed area of quantitation. Postnatal nYap⁺ cell distribution quantitation was
704 done by binning the CA1 region into mono-layer apical edge, ventricular-subventricular
705 zone (vz/svz) and the remaining area that includes the white matter (*stratum oriens*) and

the pyramidal layer. Confocal stacks of immuno-stained sections of each developmental stage were generated by scanning at intervals of 0.99 μ m using filters of appropriate wavelengths at 20X, 40X, 63X and 100X magnifications. Representative images for cell adhesion molecules corresponded to one 0.99 μ m-thick confocal plane. Measurements for labeling index (n=7/genotype), quit fraction (n=12/genotype), birth-dating studies (n=5/genotype), TUNEL cell counts (n=7 hemi-sections/genotype/condition), P0 Tbr2⁺ basal progenitor cell counts (n=7/genotype/condition) were calculated using ImageJ. Statistical significance was assessed using 2-tailed unpaired t-tests with Welch's correction (for medial length measurements, labeling index, quit fraction and progenitor cell counts, birth-dating experiments) and ANOVA followed by Tukey post-test (one-way ANOVA for critical period CA1 length, TUNEL counts and total P3 nYap⁺ cell counts; two-way ANOVA for P0 total nYap⁺ and Tbr2⁺ cell counts, and nYap⁺ cell distribution post-verteporfin treatment). These analyses were performed in GraphPad Prism v7.0 (GraphPad Software Inc., San Diego, USA) and in Microsoft Excel. Differences were considered significant at p<0.05. Data are represented as mean \pm SEM for Figures 2,5,7, Figure 1 – figure supplement 3, Figure 2 – figure supplement 1, Figure 3 – figure supplement 1 and Figure 7 – figure supplement 2. ARRIVE guidelines have been followed for reporting work involving animal research.

DATA AVAILABILITY

RNA-seq data is deposited to the Gene Expression Omnibus (GSE127896).

ACKNOWLEDGMENT

729 We thank Jean J. Zhao for gifts of mouse lines (*GFAP-cre* and *Rosa26-rtTA*;
730 *Pik3ca*^{H1047R}); William B. Dobyns and Chris Brewer for discussions. The mouse anti-
731 Pax6 antibody developed by Kawakami A., was obtained from the Developmental
732 Studies Hybridoma Bank (DSHB), created by the NICHD of the NIH and maintained at
733 The University of Iowa, Department of Biology, Iowa City, IA 52242.

734

735 **FUNDING SOURCES**

736 This work is funded by Seattle Children's Hydrocephalus Research Guild seed fund and
737 NIH grant 1R01NS099027 (KJM), and NIH Eunice Kennedy Shriver National Institute of
738 Child Health and Human Development U54HD083091 (UW Intellectual and
739 Developmental Disabilities Research Center Genetics Core).

References

- Adamsbaum C, Robain O, Cohen PA, Delalande O, Fohlen M, Kalifa G (1998) Focal cortical dysplasia and hemimegalencephaly: histological and neuroimaging correlations. *Pediatr Radiol* 28:583-590.
- Baek ST, Copeland B, Yun E-J, Kwon S-K, Guemez-Gamboa A, Schaffer AE, Kim S, Kang H-C, Song S, Mathern GW, Gleeson JG (2015) An AKT3-FOXG1-reelin network underlies defective migration in human focal malformations of cortical development. *Nat Med* 21:1445-1454.
- Belteki G, Haigh J, Kabacs N, Haigh K, Sison K, Costantini F, Whitsett J, Quaggin SE, Nagy A (2005) Conditional and inducible transgene expression in mice through the combinatorial use of Cre-mediated recombination and tetracycline induction. *Nucleic acids research* 33:e51.
- Borrell V (2018) How Cells Fold the Cerebral Cortex. *J Neurosci* 38:776-783.
- Brodowska K, Al-Moujahed A, Marmalidou A, Meyer Zu Horste M, Cichy J, Miller JW, Gragoudas E, Vavvas DG (2014) The clinically used photosensitizer Verteporfin (VP) inhibits YAP-TEAD and human retinoblastoma cell growth in vitro without light activation. *Experimental eye research* 124:67-73.
- Camargo Ortega G, Falk S, Johansson PA, Peyre E, Broix L, Sahu SK, Hirst W, Schlichthaerle T, De Juan Romero C, Draganova K, Vinopal S, Chinnappa K, Gavranovic A, Karakaya T, Steininger T, Merl-Pham J, Feederle R, Shao W, Shi SH, Hauck SM, Jungmann R, Bradke F, Borrell V, Geerloff A, Reber S, Tiwari VK, Huttner WB, Wilsch-Brauninger M, Nguyen L, Gotz M (2019) The centrosome protein AKNA regulates neurogenesis via microtubule organization. *Nature* 567:113-117.
- Carracedo A, Pandolfi PP (2008) The PTEN-PI3K pathway: of feedbacks and cross-talks. *Oncogene* 27:5527-5541.
- D'Arcangelo G, Miao GG, Chen SC, Soares HD, Morgan JI, Curran T (1995) A protein related to extracellular matrix proteins deleted in the mouse mutant reeler. *Nature* 374:719-723.
- D'Gama AM, Woodworth MB, Hossain AA, Bizzotto S, Hatem NE, LaCoursiere CM, Najm I, Ying Z, Yang E, Barkovich AJ, Kwiatkowski DJ, Vinters HV, Madsen JR, Mathern GW, Blumcke I, Poduri A, Walsh CA (2017) Somatic Mutations Activating the mTOR Pathway in Dorsal Telencephalic Progenitors Cause a Continuum of Cortical Dysplasias. *Cell Rep* 21:3754-3766.
- Davis S, Meltzer PS (2007) GEOquery: a bridge between the Gene Expression Omnibus (GEO) and BioConductor. *Bioinformatics* 23:1846-1847.
- de Juan Romero C, Bruder C, Tomasello U, Sanz-Anquela JM, Borrell V (2015) Discrete domains of gene expression in germinal layers distinguish the development of gyrencephaly. *EMBO J* 34:1859-1874.
- Fan R, Kim NG, Gumbiner BM (2013) Regulation of Hippo pathway by mitogenic growth factors via phosphoinositide 3-kinase and phosphoinositide-dependent kinase-1. *Proc Natl Acad Sci U S A* 110:2569-2574.
- Fernandez V, Llinares-Benadero C, Borrell V (2016) Cerebral cortex expansion and folding: what have we learned? *EMBO J* 35:1021-1044.
- Furey CG, Choi J, Jin SC, Zeng X, Timberlake AT, Nelson-Williams C, Mansuri MS, Lu Q, Duran D, Panchagnula S, Allocco A, Karimy JK, Khanna A, Gaillard JR, DeSpenza T, Antwi P, Loring E, Butler WE, Smith ER, Warf BC, Strahle JM, Limbrick DD, Storm PB, Heuer G, Jackson EM, Iskandar BJ, Johnston JM, Tikhonova I, Castaldi C, Lopez-Giraldez F, Bjornson RD, Knight JR, Bilguvar K, Mane S, Alper SL, Haider S, Guclu B, Bayri Y, Sahin Y, Apuzzo MLJ, Duncan CC, DiLuna ML, Gunel M, Lifton RP, Kahle KT (2018) De Novo Mutation in Genes Regulating Neural Stem Cell Fate in Human Congenital Hydrocephalus. *Neuron* 99:302-314 e304.
- Geering B, Cutillas PR, Nock G, Gharbi SI, Vanhaesebroeck B (2007) Class IA phosphoinositide 3-kinases are obligate p85-p110 heterodimers. *Proc Natl Acad Sci U S A* 104:7809-7814.

786 Gout I, Dhand R, Panayotou G, Fry MJ, Hiles I, Otsu M, Waterfield MD (1992) Expression and
787 characterization of the p85 subunit of the phosphatidylinositol 3-kinase complex and a related
788 p85 beta protein by using the baculovirus expression system. *The Biochemical journal* 288 (Pt
789 2):395-405.

790 Grant SG, O'Dell TJ, Karl KA, Stein PL, Soriano P, Kandel ER (1992) Impaired long-term potentiation,
791 spatial learning, and hippocampal development in fyn mutant mice. *Science* 258:1903-1910.

792 Gregory MD, Kippenhan JS, Dickinson D, Carrasco J, Mattay VS, Weinberger DR, Berman KF (2016)
793 Regional Variations in Brain Gyrification Are Associated with General Cognitive Ability in
794 Humans. *Curr Biol* 26:1301-1305.

795 Guerra MM, Henzi R, Ortloff A, Lichtin N, Vio K, Jimenez AJ, Dominguez-Pinos MD, Gonzalez C, Jara MC,
796 Hinostroza F, Rodriguez S, Jara M, Ortega E, Guerra F, Sival DA, den Dunnen WF, Perez-Figares
797 JM, McAllister JP, Johanson CE, Rodriguez EM (2015) Cell Junction Pathology of Neural Stem
798 Cells Is Associated With Ventricular Zone Disruption, Hydrocephalus, and Abnormal
799 Neurogenesis. *Journal of neuropathology and experimental neurology* 74:653-671.

800 Gumbiner BM, Kim NG (2014) The Hippo-YAP signaling pathway and contact inhibition of growth. *J Cell*
801 *Sci* 127:709-717.

802 Gymnopoulos M, Elsliger MA, Vogt PK (2007) Rare cancer-specific mutations in PIK3CA show gain of
803 function. *Proc Natl Acad Sci U S A* 104:5569-5574.

804 Hansen CG, Moroishi T, Guan KL (2015) YAP and TAZ: a nexus for Hippo signaling and beyond. *Trends in*
805 *cell biology* 25:499-513.

806 Huang TS, Li L, Moalim-Nour L, Jia D, Bai J, Yao Z, Bennett SA, Figeys D, Wang L (2015) A Regulatory
807 Network Involving beta-Catenin, e-Cadherin, PI3k/Akt, and Slug Balances Self-Renewal and
808 Differentiation of Human Pluripotent Stem Cells In Response to Wnt Signaling. *Stem Cells*
809 33:1419-1433.

810 Jansen LA, Mirzaa GM, Ishak GE, O'Roak BJ, Hiatt JB, Roden WH, Gunter SA, Christian SL, Collins S,
811 Adams C, Riviere JB, St-Onge J, Ojemann JG, Shendure J, Hevner RF, Dobyns WB (2015) PI3K/AKT
812 pathway mutations cause a spectrum of brain malformations from megalencephaly to focal
813 cortical dysplasia. *Brain* 138:1613-1628.

814 Jimenez AJ, Dominguez-Pinos MD, Guerra MM, Fernandez-Llebrez P, Perez-Figares JM (2014) Structure
815 and function of the ependymal barrier and diseases associated with ependyma disruption.
816 *Tissue barriers* 2:e28426.

817 Jimenez AJ, Garcia-Verdugo JM, Gonzalez CA, Batiz LF, Rodriguez-Perez LM, Paez P, Soriano-Navarro M,
818 Roales-Bujan R, Rivera P, Rodriguez S, Rodriguez EM, Perez-Figares JM (2009) Disruption of the
819 neurogenic niche in the subventricular zone of postnatal hydrocephalic hyh mice. *Journal of*
820 *neuropathology and experimental neurology* 68:1006-1020.

821 Kadowaki M, Nakamura S, Machon O, Krauss S, Radice GL, Takeichi M (2007) N-cadherin mediates
822 cortical organization in the mouse brain. *Dev Biol* 304:22-33.

823 Keppler-Noreuil KM, Sapp JC, Lindhurst MJ, Parker VE, Blumhorst C, Darling T, Tosi LL, Huson SM,
824 Whitehouse RW, Jakkula E, Grant I, Balasubramanian M, Chandler KE, Fraser JL, Gucev Z, Crow
825 YJ, Brennan LM, Clark R, Sellars EA, Pena LD, Krishnamurty V, Shuen A, Braverman N,
826 Cunningham ML, Sutton VR, Tasic V, Graham JM, Jr., Geer J, Jr., Henderson A, Semple RK,
827 Biesecker LG (2014) Clinical delineation and natural history of the PIK3CA-related overgrowth
828 spectrum. *Am J Med Genet A* 164A:1713-1733.

829 Khan F, Rehman A, Shamim MS, Bari ME (2015) Factors affecting ventriculoperitoneal shunt survival in
830 adult patients. *Surgical neurology international* 6:25.

831 Kostic M, Paridaen J, Long KR, Kalebic N, Langen B, Grubling N, Wimberger P, Kawasaki H, Namba T,
832 Huttner WB (2019) YAP Activity Is Necessary and Sufficient for Basal Progenitor Abundance and
833 Proliferation in the Developing Neocortex. *Cell Rep* 27:1103-1118 e1106.

834 Lavado A, Oliver G (2011) Six3 is required for ependymal cell maturation. *Development* 138:5291-5300.
 835 Lavado A, Park JY, Pare J, Finkelstein D, Pan H, Xu B, Fan Y, Kumar RP, Neale G, Kwak YD, McKinnon PJ,
 836 Johnson RL, Cao X (2018) The Hippo Pathway Prevents YAP/TAZ-Driven Hypertranscription and
 837 Controls Neural Progenitor Number. *Developmental cell* 47:576-591 e578.
 838 Lewitus E, Kelava I, Kalinka AT, Tomancak P, Huttner WB (2014) An adaptive threshold in mammalian
 839 neocortical evolution. *PLoS biology* 12:e1002000.
 840 Liu-Chittenden Y, Huang B, Shim JS, Chen Q, Lee SJ, Anders RA, Liu JO, Pan D (2012) Genetic and
 841 pharmacological disruption of the TEAD-YAP complex suppresses the oncogenic activity of YAP.
 842 *Genes Dev* 26:1300-1305.
 843 Liu P, Cheng H, Santiago S, Raeder M, Zhang F, Isabella A, Yang J, Semaan DJ, Chen C, Fox EA, Gray NS,
 844 Monahan J, Schlegel R, Beroukhim R, Mills GB, Zhao JJ (2011) Oncogenic PIK3CA-driven
 845 mammary tumors frequently recur via PI3K pathway-dependent and PI3K pathway-independent
 846 mechanisms. *Nat Med* 17:1116-1120.
 847 Llinares-Benadero C, Borrell V (2019) Deconstructing cortical folding: genetic, cellular and mechanical
 848 determinants. *Nature reviews Neuroscience*.
 849 Madisen L, Zwingman TA, Sunkin SM, Oh SW, Zariwala HA, Gu H, Ng LL, Palmiter RD, Hawrylycz MJ,
 850 Jones AR, Lein ES, Zeng H (2010) A robust and high-throughput Cre reporting and
 851 characterization system for the whole mouse brain. *Nat Neurosci* 13:133-140.
 852 Martinez JM, Wang HZ, Lin RZ, Brink PR, White TW (2015) Differential regulation of Connexin50 and
 853 Connexin46 by PI3K signaling. *FEBS letters* 589:1340-1345.
 854 McCarthy DJ, Smyth GK (2009) Testing significance relative to a fold-change threshold is a TREAT.
 855 *Bioinformatics* 25:765-771.
 856 Mirzaa GM, Conway RL, Gripp KW, Lerman-Sagie T, Siegel DH, deVries LS, Lev D, Kramer N, Hopkins E,
 857 Graham JM, Jr., Dobyns WB (2012) Megalencephaly-capillary malformation (MCAP) and
 858 megalencephaly-polydactyly-polymicrogyria-hydrocephalus (MPPH) syndromes: two closely
 859 related disorders of brain overgrowth and abnormal brain and body morphogenesis. *Am J Med*
 860 *Genet A* 158A:269-291.
 861 Morales DM, Townsend RR, Malone JP, Ewersmann CA, Macy EM, Inder TE, Limbrick DD, Jr. (2012)
 862 Alterations in protein regulators of neurodevelopment in the cerebrospinal fluid of infants with
 863 posthemorrhagic hydrocephalus of prematurity. *Mol Cell Proteomics* 11:M111 011973.
 864 Nagasaka A, Shinoda T, Kawaue T, Suzuki M, Nagayama K, Matsumoto T, Ueno N, Kawaguchi A, Miyata T
 865 (2016) Differences in the Mechanical Properties of the Developing Cerebral Cortical Proliferative
 866 Zone between Mice and Ferrets at both the Tissue and Single-Cell Levels. *Frontiers in cell and*
 867 *developmental biology* 4:139.
 868 Najib S, Saint-Laurent N, Esteve JP, Schulz S, Boutet-Robinet E, Fourmy D, Lattig J, Mollereau C, Pyronnet
 869 S, Susini C, Bousquet C (2012) A switch of G protein-coupled receptor binding preference from
 870 phosphoinositide 3-kinase (PI3K)-p85 to filamin A negatively controls the PI3K pathway. *Mol Cell*
 871 *Biol* 32:1004-1016.
 872 Park JH, Shin JE, Park HW (2018) The Role of Hippo Pathway in Cancer Stem Cell Biology. *Molecules and*
 873 *cells* 41:83-92.
 874 Park R, Moon UY, Park JY, Hughes LJ, Johnson RL, Cho SH, Kim S (2016) Yap is required for ependymal
 875 integrity and is suppressed in LPA-induced hydrocephalus. *Nat Commun* 7:10329.
 876 Parrini E, Conti V, Dobyns WB, Guerrini R (2016) Genetic Basis of Brain Malformations. *Molecular*
 877 *syndromology* 7:220-233.
 878 Patro R, Duggal G, Love MI, Irizarry RA, Kingsford C (2017) Salmon provides fast and bias-aware
 879 quantification of transcript expression. *Nature methods* 14:417-419.
 880 Reillo I, Borrell V (2012) Germinal zones in the developing cerebral cortex of ferret: ontogeny, cell cycle
 881 kinetics, and diversity of progenitors. *Cereb Cortex* 22:2039-2054.

882 report VVIF (2000), p
 883 https://www.accessdata.fda.gov/drugsatfda_docs/label/2012/021119s021022lbl.pdf.
 884 Ritchie ME, Phipson B, Wu D, Hu Y, Law CW, Shi W, Smyth GK (2015) limma powers differential
 885 expression analyses for RNA-sequencing and microarray studies. *Nucleic acids research* 43:e47.
 886 Robinson MD, McCarthy DJ, Smyth GK (2010) edgeR: a Bioconductor package for differential expression
 887 analysis of digital gene expression data. *Bioinformatics* 26:139-140.
 888 Ronan L, Fletcher PC (2015) From genes to folds: a review of cortical gyrification theory. *Brain structure*
 889 & function 220:2475-2483.
 890 Roy A, Skibo J, Kalume F, Ni J, Rankin S, Lu Y, Dobyns WB, Mills GB, Zhao JJ, Baker SJ, Millen KJ (2015)
 891 Mouse models of human PIK3CA-related brain overgrowth have acutely treatable epilepsy. *Elife*
 892 4.
 893 Schmidt-Erfurth U, Hasan T (2000) Mechanisms of action of photodynamic therapy with verteporfin for
 894 the treatment of age-related macular degeneration. *Survey of ophthalmology* 45:195-214.
 895 Schnitzer J, Franke WW, Schachner M (1981) Immunocytochemical demonstration of vimentin in
 896 astrocytes and ependymal cells of developing and adult mouse nervous system. *J Cell Biol*
 897 90:435-447.
 898 Sonesson C, Love MI, Robinson MD (2015) Differential analyses for RNA-seq: transcript-level estimates
 899 improve gene-level inferences. *F1000Research* 4:1521.
 900 Tran NL, Adams DG, Vaillancourt RR, Heimark RL (2002) Signal transduction from N-cadherin increases
 901 Bcl-2. Regulation of the phosphatidylinositol 3-kinase/Akt pathway by homophilic adhesion and
 902 actin cytoskeletal organization. *J Biol Chem* 277:32905-32914.
 903 Tully HM, Dobyns WB (2014) Infantile hydrocephalus: a review of epidemiology, classification and
 904 causes. *Eur J Med Genet* 57:359-368.
 905 Tully HM, Ishak GE, Rue TC, Dempsey JC, Browd SR, Millen KJ, Doherty D, Dobyns WB (2016) Two
 906 Hundred Thirty-Six Children With Developmental Hydrocephalus: Causes and Clinical
 907 Consequences. *J Child Neurol* 31:309-320.
 908 Yung YC, Stoddard NC, Mirendil H, Chun J (2015) Lysophosphatidic Acid signaling in the nervous system.
 909 *Neuron* 85:669-682.
 910 Zhao L, Vogt PK (2008) Helical domain and kinase domain mutations in p110alpha of
 911 phosphatidylinositol 3-kinase induce gain of function by different mechanisms. *Proc Natl Acad*
 912 *Sci U S A* 105:2652-2657.
 913 Zhuo L, Theis M, Alvarez-Maya I, Brenner M, Willecke K, Messing A (2001) hGFAP-cre transgenic mice for
 914 manipulation of glial and neuronal function in vivo. *Genesis* 31:85-94.

915

FIGURE LEGENDS

Figure 1: Embryonic induction of *Pik3ca*^{H1047R} activating mutation causes cortical gyrification in mice

(a-d) Nissl-stained coronal sections of P3 control and *GFAP-cre;Pik3ca*^{H1047R} mutant hemi-forebrains revealed hippocampal (dotted lines) and neocortical gyrification (open arrowheads), when induced embryonically. (e,f) 3D models of control and mutant hippocampi. (g-l) Gross patterning of all hippocampal substructures was intact, as shown by *Ctip2*, *Satb2* and *Tbr1* expression. Medial gyrification was restricted primarily to the mutant CA1 region. CA – cornus ammonis (red dotted line, a-d); sub – subiculum; DG – dentate gyrus (blue dotted line, a-d; g-j). Scale bars: 1mm (a-d), 100μm (n-s). See also Figure 1 – figure supplements 1-3.

Figure 2: Altered neurogenesis in *Pik3ca* mutant at embryonic and postnatal stages follows the stereotypic cortical ‘gyrification sequence’

(a) Schematics of E14.5 and E16.5 coronal hemi-section, boxes represent region of interest (b,d,f,h,j). Images are oriented with lateral neocortex on the top, followed by lateral ventricle (LV) and then CA1 (b,d,f,h,j,l-o’). (b-e) Compared to control, E14.5 *Pik3ca*^{H1047R} mutants exhibited significantly higher labeling index, indicating higher proliferation rate. Though E16.5 mutant CA1 showed no overt change in labeling index, pHH3⁺ cells marking the M-phase appeared to be ectopic (yellow arrowheads), indicating early mis-localization of dividing cells. (f-i) Compared with respective controls, E14.5 and E16.5 *GFAP-cre;Pik3ca*^{H1047R} mutants, induced from E0.5, showed significant increase in primary (apical Sox2⁺Tbr2⁻, aRGs) and secondary (Tbr2⁺ IPs;

939 basal Sox2⁺Tbr2⁻, bRGs) progenitor pools, in accordance with the gyrification sequence;
940 yellow circle marks bRG. Data are normalized and represented as mean ± SEM in
941 scatter plots; 2-tailed unpaired t-tests were performed (c,e,g,i). (j,k) Cell cycle exit
942 during the E15.5-E16.5 period was significantly higher in the mutant CA1 than the
943 control, as represented in mean ± SEM scatter plots (t=10.16, degrees of freedom
944 (df)=21.73). (l-m') Compared to controls, P3 mutant CA1 region showed focal increase
945 in Pax6⁺ and Tbr2⁺ progenitors at the gyral ventricular-subventricular zone; the apical
946 edge remained predominantly unfolded. (n-o') Nestin⁺ and GFAP⁺ intermediate
947 filaments in P3 were misoriented and divergent from focal points (asterisks) at the
948 mutant gyri. (p) Schematics of P3 control and mutant hemi-sections; boxes depict
949 regions shown in l-o'. Differences were considered significant at p<0.05; ns, not
950 significant. nctx, neocortex; PL, pyramidal layer. Scale bars: 50µm (b,d,f,h,j), 100µm (l-
951 o'). See also Figure 2 – figure supplement 1.

952 **Figure 3: Non-random gyrification pattern in *Pik3ca*^{H1047R} mutant has a narrow**
953 **embryonic critical period**

954 (a-j) Nissl-stained coronal hemi-sections depicting hippocampal morphology, alongside
955 schematics (e,j). Compared to control (a), *Pik3ca*^{H1047R} mutant hippocampus showed
956 graded severity in gyrification, depending on the time and duration of mutation
957 induction. The critical period of the most severe folding with a non-random folding
958 pattern ends at E15.5 (b-d). Postnatal induction of *Pik3ca*^{H1047R} mutation is not effective
959 to cause cortical gyrification (i). (k) Developmental timeline of mutation induction and
960 the corresponding hippocampal gyrification phenotype. Scale bars: 1mm (a-d, f-i). See
961 also Figure 3 – figure supplement 1.

Figure 4: Embryonic induction of *Pik3ca*^{H1047R} mutation causes early disruption of apical cell adhesion

(a,j) Schematic of E14.5 and E16.5 hemi-section showing area of interest. (b-i) Compared to control, E16.5 *Pik3ca*^{H1047R} mutant, induced from E0.5, showed abnormal zippering of forebrain apical membranes (open arrowheads, f-h), with XZ plane indicating subtle mis-localization of cell adhesion molecules β -Catenin and ZO-1 (d,h). N-Cadherin, that is normally expressed uniformly at the juxtaposition of the apical membranes (e), appeared to be clustered around the unzipped portion and sporadically absent (asterisk) in adjacent parts of the membrane junction (i). (k-r) Compared to control, CA1 ventricular lining of E14.5 mutant showed subtle disruption in the localization of β -Catenin, N-Cadherin, ZO1, as marked by white arrows (o-q) and asterisk (r). bv – blood vessels. Scalebars: 20 μ m (b-i,k-r). See also Figure 4 – figure supplement 1.

Figure 5: Embryonic induction of *Pik3ca*^{H1047R} mutation disrupts early developing ependyma and induces increase in nYap⁺ cells

(a,n) Schematics of P3, E16.5 and E14.5 hemi-sections; boxed regions depict areas of interest. (b-d,o,o'p,s,s') Ependymal markers Yap and Vimentin, and junction protein ZO-1 are localized at the apical lining of P3, E16.5 and E14.5 control CA1 respectively. Additionally, Yap and ZO-1 mark the blood vessel membranes (bv), while Vimentin mark the hippocampal radial glia. (e) P0 mutant CA1 gyral ventricular lining showed presence of focal nYap-enriched zones (arrowheads, orange box), interspersed by Yap-

sparse zones at the sulci (cyan box). **(f,i)** Increased Yap⁺ nuclei in P3 mutant gyri (open arrowheads) and Yap-sparse mutant sulcus edge (asterisks) indicated disrupted ependyma. **(g,j)** ZO-1 was ectopically expressed in P3 mutant gyral ventricular zone, with breaks in the sulcus areas. **(h,k)** Vimentin⁺ fibers appeared to be arranged in an hour-clock pattern at the gyri; sulci demonstrated more disoriented fibers and gaps (asterisk); dashed lines mark the basal ependymal edge. **(l,m)** Total number and distribution of nYap⁺ cells in the different CA1 subzones (binned as mono-layer apical edge, ventricular-subventricular zone (vz/svz), white matter (wm) and CA1 pyramidal layer (CA1 PL)) were significantly enhanced in P3 mutant, compared to control littermates (total counts: F=179.1, df=28; cell distribution: F=137.8, df=86). The control CA1 showed minimal existence of nYap⁺ cells beyond the vz/svz. Data are represented as mean ± SEM in scatter plots (l) or 100% stacked columns (m); one-way and two-way ANOVA were performed respectively. **(o-q')** Compared with control, E16.5 *Pik3ca*^{H1047R} mutant showed abnormal zippering of forebrain apical membranes, combined with focal nYap expression (arrowheads). **(s-t')** Compared with control, E14.5 mutant medial apical membrane showed subtle disruption of cell adhesion causing minor buckling/unevenness. Magnified images of E14.5 and E16.5 ventricular edge demonstrated higher number of nYap⁺ cells in the mutant (yellow dotted lines) compared to controls (o',q',s',t'); some non-nYap⁺ cells are marked with pink dotted lines for the purpose of comparison (o',s',t'). Scale bars: 20μm (b-d, f-k, o-t), 500μm (e), 10μm (o',q',s',t'). See also Figure 5 – figure supplement 1.

Figure 6: Translocation of Yap from nucleus to cytoplasm by verteporfin attenuates gyrification and ventriculomegaly in *Pik3ca*^{H1047R} mutant

(a) Developmental timeline of verteporfin administration (E13.5>E18.5). (b-d) Nissl-staining revealed attenuation of gyrification and absence of ventriculomegaly in P0 *Pik3ca*^{H1047R} mutant (induced E13.5>E15.5) post-verteporfin administration. Boxes mark the respective areas of interest for (e-g). (e-g) Flowchart of laser capture microdissection (LCM) of marked ventricular-subventricular zone tissue samples, and RNA sequencing. Asterisks (c,f) mark neocortical gyrification in the untreated mutant brains, that were also eventually attenuated by verteporfin (d,g). (h) Principal component (PC) analysis revealed that verteporfin administration drives ventricular *Pik3ca* mutant gene expression towards that of control tissue. PC1 is largely explained by PI3K signaling, PC2 by Hippo-Yap signaling. (i) Graphs showing the effect of PI3K overactivation and of verteporfin treatment in *Pik3ca*. Scale bars: 1mm (b-d), 500µm (e-g). See also Figure 6 – figure supplements 1-3, Figure 6 – Source Data 1 and 2.

Figure 7: Reduction of nYap by verteporfin re-establishes developing apical junctions and suppresses focal proliferation in *Pik3ca*^{H1047R} mutant

(a) Schematics of P0 control and mutant (+/- verteporfin) forebrain hemi-sections; boxes depict respective areas of interest. (b-g) P0 control untreated brain expressed cYap, adherens junction protein ZO-1 and radial glial markers Vimentin and Nestin, uniformly along the juxtaposed apical membranes. Ctip2 and Tbr2 were expressed in pyramidal neurons and IPs respectively. (h-s') Verteporfin treatment significantly normalized Yap localization, from nucleus to cytoplasm, restored apical junctions and streamlined

disrupted radial glial scaffold, as compared to the untreated P0 (dox E13.5>E15.5) mutant gyri and sulci. (t,u) The treatment significantly reduced the total nYap⁺ cell number in the mutant hippocampal gyri and sulci (F=70.47, df=32) as well as normalized the nYap⁺ cell distribution to the control levels (F=134.4, df96). This also significantly decreased the Tbr2⁺ progenitor population (F=31.45, df= 35), especially in the mutant gyral zones, as quantitated in (v). This resulted in attenuation of the extent of gyrification and re-zipping of the apical membranes to halt the progressive ventriculomegaly. Data are represented as mean \pm SEM in scatter plots (t); two-way ANOVA was followed by Tukey's post-tests. ns, not significant. Open arrowheads, disrupted/ectopic junctional and endymal proteins in mutant; asterisks, absence of adhesion/endymal molecules at the mutant apical edge; arrowheads, rescued apical ventricular lining in the mutant post-verteporfin treatment; bv, blood vessels; LV, lateral ventricle. Scalebars: 20 μ m (b-s'). See also Figure 7 – figure supplements 1-2.

Figure 8: Summary: PI3K-Yap gyrification model

(a) Schematic of PI3K-AKT-MTOR pathway, its connection with Yap signaling and mode of verteporfin action. The activity of the PI3K enzyme (dimer of catalytic and regulatory subunits) initiates the PI3K-AKT-MTOR pathway cascade. In parallel, downstream of the Hippo pathway, Yap binds to transcriptional regulator proteins in the nucleus, to facilitate cell growth and proliferation. Activation of Hippo pathway results in translocation of nuclear Yap to cytoplasm through phosphorylation. Cytoplasmic Yap, in turn, promotes cell adhesion. The activating *Pik3ca* mutation results in Yap translocation from cytoplasm to nucleus, possibly via Pdk1. In this study, verteporfin, a

1054 nuclear Yap inhibitor, restored cytoplasmic Yap. **(b,c)** Schematics summarizing main
1055 findings of the paper: PI3K over-activation resulted in disruption of cell adhesion at the
1056 neural-ependymal transition zone causing ventriculomegaly, and also in differential
1057 proliferation of progenitors, thus triggering the gyrification sequence cascade (effect of
1058 genotype). In mutant mice, verteporfin attenuated these anomalies (effect of drug),
1059 leading to reduction in gyrification severity as well as ventriculomegaly. Area within the
1060 yellow dashed boxes in the top rows of (b) and (c) is magnified in the respective bottom
1061 rows. Color coding for elements in (b) and (c) is explained in the figure “key”.
1062 vz/svz, ventricular/subventricular zone.

Figure supplements:

Figure 1 – figure supplement 1: Genetic strategy for *Pik3ca*^{H1047R} mouse model and expression of *GFAP-cre* line

(a) Schematic of *PIK3CA* functional domains, highlighting position of the *H1047R* activating mutation, modified from Roy et al., 2015.(Roy et al., 2015) (b) Genetic strategy for tet-activated *Pik3ca*^{H1047R} *transgenic* mice (Liu et al., 2011): the human *Pik3ca*^{H1047R} mutation was activated in the combined presence of *cre* recombinase and doxycycline (dox). rtTA, reverse tetracycline-controlled trans-activator. (c,d) *GFAP-cre* expression, using Ai14 reporter line at E14.5 and E16.5, is stronger in medial telencephalon, compared to lateral telencephalon; boxes represent region of interest. Nctx, neocortex; LV, lateral ventricle, CA, cornus ammonis; DG, dentate gyrus. Scale bar: 500µm, 1mm (c)

Figure 1 – figure supplement 2: Characterization of true gyrification in *Pik3ca*^{H1047R} mutant neocortex and hippocampus

(a-e, k-o) In control lissencephalic postnatal mouse brain, the ventricular (apical) and pial (basal) surfaces of both neocortex and hippocampus are smooth and parallel to each other, with no apparent difference in thickness within any intermediate cell layer or white matter (green arrows (b,d,l,n)). This is demonstrated using Nissl staining (a,k) and in schematics (e,j). Ctip2, Satb2 differentially mark the cortical plate (CP) and hippocampal pyramidal layer (CA1 PL) on either side of the lateral ventricle (LV). (f-j,p-t) Postnatal *GFAP-cre;Pik3ca*^{H1047R} mutant mouse brain demonstrated the criteria of true gyrification (Borrell, 2018) both in the lateral neocortex and in the hippocampal

CA1, as demonstrated in schematics (j,t). Nissl staining and immunohistochemical analyses revealed folding of mutant pial surface, white matter (wm) and the neuronal layers (CP, CA1 PL) but predominantly smooth apical ventricular surfaces. The relative thickness of mutant gyri (folds distal to the ventricle; yellow/orange arrows) was greater compared to that of the adjacent mutant sulci (folds proximal to the ventricle; blue arrows) – property observed in normal gyrencephalic mammals. Point to be noted: the *Pik3ca*^{H1047R} mutant brain also demonstrated some extent of neuronal migration defect (this study; (Roy et al., 2015)). In all the panels, solid line marks ventricular edge; dashed lines distinguish progenitor zone, white matter and neuronal zone, while dotted line marks the pial edge. In schematics (e,j,o,t), pial surface is purple, neuronal plate is blue, white matter is light yellow, ventricular-subventricular zone is pink. slm – *stratum lacunosum-moleculare*, so – *stratum oriens*. Scale bars: 200µm (a-d,f-l,k-n,p-s).

Figure 1 – figure supplement 3: *Pik3ca*^{H1047R} mutant demonstrates increase in ventricular length

(a,c,e) Nissl-stained coronal sections of P3, E14.5 and E16.5 control and *Pik3ca*^{H1047R} mutant forebrains, induced by doxycycline from E0.5. (b) Normalized lengths of P3 CA1 and dentate gyrus (DG) measured as shown by red and blue dotted lines respectively in (a), were significantly longer in the mutant, compared to control (CA1: t=6.372, df=7.197; DG: t=2.698, df=7.165). (d,f) Normalized length of the medial ventricular lining, measured as shown in (c,e) by dotted lines in the control (yellow dotted line) and mutant (red dotted line) embryos, was significantly longer in the mutant, compared to control at both E14.5 (t=4.065, df=11.16) and E16.5 (t=8.267, df=14.4). Open arrowheads marked the occurrence of cortical folds in E16.5 mutant forebrain. Data are

represented as mean \pm SEM in scatter plots; 2-tailed unpaired t-tests were performed (b,d,f). Scale bars: 1mm (a), 300 μ m (c), 500 μ m (e).

Figure 2 – figure supplement 1: *Pik3ca*^{H1047R} mutant demonstrates normal cell fate specification but disrupted neural scaffold and migration

(a) Experimental outline of birth-dating assay: BrdU was injected at E16.5 and analyzed at P0 (B16.5;P0). (b,c) At P0, total numbers of Ctip2⁺ cells, of cells born at E16.5 (BrdU⁺), and of Ctip2⁺ cells generated at E16.5 (Ctip2⁺/BrdU⁺; d) were not significantly different between respective controls and *Pik3ca*^{H1047R} mutant CA1 regions, indicating no effect of PI3K overactivation on cell fate specification in CA1. Data are represented as mean \pm SEM in scatter plots; 2-tailed unpaired t-tests were performed (Ctip2⁺: t=0.7623, df=10.24; BrdU⁺: t=0.8534, df=6.91; BrdU⁺Ctip2⁺: t=1.752, df=6.61; b-d). Differences were considered significant at p<0.05; ns, not significant. (e-j) Nestin⁺ radial glial fibers appeared slightly irregular in E14.5 *Pik3ca*^{H1047R} mutant (f) but became progressively hyper-fasciculated and dysplastic morphology at E16.5 (d,i) compared to respective controls (e,g,i). The Laminin⁺ mutant basement membrane was thinner at E14.5 and thicker at E16.5, compared to respective controls. Also, E16.5 mutant PL was widely dispersed and showed severe reduction of the *stratum lacunosum-moleculare* (slm; j). (k) Schematics of E14.5, E16.5 (boxes marked regions shown in (e-j)) and P2 hemi-sections. (l,m) Calbindin⁺ cells that normally aligned along the ventricular side of P2 control CA1 PL (arrowheads), were severely dispersed (open arrowheads), clustering around the white matter of mutant gyral area. (n,o) Compared

to control, P2 mutant displayed more Reelin⁺ cells along the gyrified neural tissue, but none were found in ectopic locations. Scale bars: 25µm (e-j, i-o).

Figure 3 – figure supplement 1: Minimal induction of PI3K overactivation is sufficient to initiate cortical folding and altered neuronal migration in E17.5 CA1

(a) Graph showing P3 CA1 length across mutants induced in graded fashion, normalized to that of the mutant induced from E0.5. Mutants induced after E15.5 showed significantly lower CA1 lengths compared to those induced before E15.5. Data are represented as mean ± SEM in scatter plots; one-way ANOVA was followed by Tukey's multiple comparison tests (F-value=20.57, df=42). (b-e) Nissl-stained coronal sections of P0 *Pik3ca*^{H1047R} mutants (doxycycline: E13.5>E14.5; E14.5>E15.5) demonstrated mild cortical dysplasia and ventriculomegaly but little gyrification, compared to respective control littermates. (f-v) E17.5 mutant, minimally induced from E13.5 to E15.5, demonstrated the first visual sign of folding, as shown in Nissl-stained coronal sections at different antero-posterior (A-P) planes (f-g",n) and when processed for Pax6, Tbr2 (h,k), Ctip2 (i,l). Region of the first undulation is marked by open arrowheads (k,l). Reelin-Laminin immunohistochemistry indicated a slightly thicker but not overtly disrupted basement membrane and a longer Reelin⁺ zone (dashed lines); however, no ectopic expression of Reelin in the mutant hippocampus was observed (j,m,r,v). Compared to controls (o,p), E17.5 *Pik3ca*^{H1047R} mutant (dox: E13.5>E15.5) showed hyper-fasciculated Nestin⁺ radial glial scaffold (s), thicker dispersed Ctip2⁺ PL with ectopic Calbindin⁺ cells (t). Mutant displayed severely reduced *stratum lacunosum-*

moleculare (slm) (asterisk; u), marked by L1 in the control section (arrowhead; q). The mutant *stratum oriens* (so) appeared normal. DG – dentate gyrus.

Scale bars: 1mm (b-e), 500µm (f-g",n), 200µm (h-m), 50µm (o-v).

Figure 4 – figure supplement 1: Disruption of apical cell adhesion caused by embryonic induction of PI3K overactivation persists postnatally

(a) Schematics of P3 control and *Pik3ca*^{H1047R} mutant; boxed areas show areas of interest. (b-d) P3 control sections showed juxtaposition of the neocortical and hippocampal apical membranes across lateral ventricles, with uniform expression and colocalization of β-Catenin and N-Cadherin (white arrows). (e-j) Comparatively, P3 mutant sulcus showed focal absence of both β-Catenin and N-Cadherin (asterisk, e-g), while the mutant gyrus demonstrated scattered areas of colocalization (open arrowheads) interspersed by solo expression of N-Cadherin and ectopic presence of cells at the non-zippered edge (h-j). Please note ventriculomegaly was highly pronounced in P3 mutant (e-j). Scale bars: 20µm (b-j).

Figure 5 – figure supplement 1: Six3⁺ cells ectopically concentrate at the mutant gyral ventricular zone

(a) Control CA1 ventricular edge did not robustly express ependymal marker Six3 at P0, although normal Six3 expression in the postmitotic layer was observed (data not shown). (b-d) P0 mutant gyri showed concentration of Six3⁺ nuclei (arrowheads), similar to the mutant nYAP expression (see Figure 5), while they are scattered in the sulci

lacking in the ventricular zone (asterisks). (e) Schematic of P0 mutant showing location of gyrus and sulcus. bv – blood vessels; LV – lateral ventricle.

Scale bars: 20 μ m (a-c), 100 μ m (d).

Figure 6 – figure supplement 1: Verteporfin administration has no overt effect on control littermates

(a-j). Verteporfin treatment did not overtly affect the normal expression of Ctip2, radial glial markers Nestin and Vimentin, intermediate progenitor marker Tbr2, cell adhesion molecules like β -Catenin, ZO-1, N-Cadherin, developing ependymal markers Yap and Six3, as well as the overall brain morphology. Box in (i) depicts area of interest. (k,l) Verteporfin treatment also did not overtly affect the Six3 expression in the developing ependyma of P0 control CA1 and mutant sulcus; however, it considerably reduced the focal concentration of Six3⁺ cells at the mutant gyral ventricular zone (asterisks). (m) Schematic of P0 mutant (verteporfin treated) showing location of gyrus and sulcus. bv – blood vessels. Scale bars: 20 μ m (a-h, j-l), 1mm (i).

Figure 6 – figure supplement 2: Barcode plots across groups showing gene enrichment

(a-d) Barcode plots showing gene enrichment of PI3K pathway and Hippo-YAP pathway for the following comparisons: mutant sulcus (no drug) versus control (no drug; $p_{PI3K}=2.02e^{-20}$, $p_{Yap}=2.35e^{-18}$), mutant gyrus (no drug) versus control (no drug; $p_{PI3K}=4.92e^{-20}$, $p_{Yap}=3.33e^{-18}$), mutant sulcus (+verteporfin) versus mutant sulcus (no drug; $p_{PI3K}=7.74e^{-19}$, $p_{Yap}=2.05e^{-17}$), and mutant gyrus (+verteporfin) versus mutant

gyrus (no drug; $p_{PI3K}=1.96e^{-19}$, $p_{Yap}=5.67e^{-18}$). The central portion of the plot shows the ranked list of all genes, ranked by p-value, with the smallest p-values to the left and the largest to the right. Genes in the set are highlighted with colored bars: red and blue bars mark upregulated and downregulated genes respectively. The “weights” show the logarithmic fold change between the two groups, giving a measure of the effect size, and the outer plots (labeled ‘Enrichment’) show the relative enrichment of the genes in the set. Thus, the enrichment plot highlights those genes that provide evidence that the whole gene set is being differentially expressed.

Figure 6 – figure supplement 3: *Pik3ca* mutant gyrification is physiologically relevant

(a) Barcode plots of a significant set of gyrification-related ferret genes (GSE60687), mapped to mouse, for the following comparisons: mutant sulcus versus control (no drug; $p=9.65e^{-21}$); mutant gyrus versus control (no drug; $p=1.57e^{-21}$), mutant sulcus versus gyrus (no drug; $p=1.64e^{-19}$). The plots indicate that top genes mapped between the ferret data and our mouse data are highly affected in our dataset. (b) Venn diagram indicates that genes relevant to normal ferret gyrification have significant overlap with those differentially expressed in the mouse mutant gyrification zones. (c) Schematics of P0 control and mutant hemi-sections, indicating regions of interest.

Figure 7 – figure supplement 1: Reduction of nYap by verteporfin re-establishes cell adhesion in *Pik3ca*^{H1047R} mutant

(a-c) Cell adhesion molecules, namely β -Catenin, N-Cadherin, were uniformly

expressed specifically along the juxtaposed apical membranes in the P0 (dox E13.5>E15.5) control brains. **(d-i')** Verteporfin treatment restored the disrupted apical cell adhesion, observed in the untreated P0 (dox E13.5>E15.5) mutant gyri and sulci. This resulted in attenuation of the extent of gyrification and re-zippering of the apical membranes to halt the progressive ventriculomegaly. **(j-l)** Schematics of P0 control and mutant (+/-Verteporfin) forebrain hemi-sections; boxes depict respective areas of interest. Asterisks, absence of adhesion/ependymal molecules at the mutant apical edge; arrowheads, rescued apical ventricular lining in the mutant post-verteporfin treatment; bv, blood vessels; LV, lateral ventricle. Scale bars: 20 μ m (a-i').

Figure 7 – figure supplement 2: Effect of verteporfin on apical junctions initiates early

(a) Developmental timeline of verteporfin administration (E13.5>E16.5). **(b,c)** Nissl-stained coronal sections of E16.5 *Pik3ca*^{H1047R} mutant and control (induced E13.5>E15.5), post-verteporfin administration, revealed similar morphology. Boxes mark the respective areas of interest. **(d-g')** Verteporfin-treated mutants demonstrated increased alignment of junctional proteins, normalized progenitor pool and reduced occurrence of unzipped apical membranes (compare with Figure 4). Dashed lines mark the apical ventricular lining. **(h)** Study of apoptosis revealed no significant differences ($F=0.3318$, $df=32$) in the number of TUNEL⁺ cells between E16.5 control and mutant (+/- Verteporfin) CA1 regions. Data is represented as mean \pm SEM in scatter plots; one-way ANOVA was performed followed by Tukey post-test. bv, blood vessels; dashed line, lateral ventricle. Scalebars: 500 μ m (b,c), 20 μ m (d-g')

1244

1245 **Video 1: 3D model of P3 control hippocampus**

1246 **Video 2: 3D model of P3 *GFAP-cre;Pik3ca*^{H1047R} hippocampus**

1247

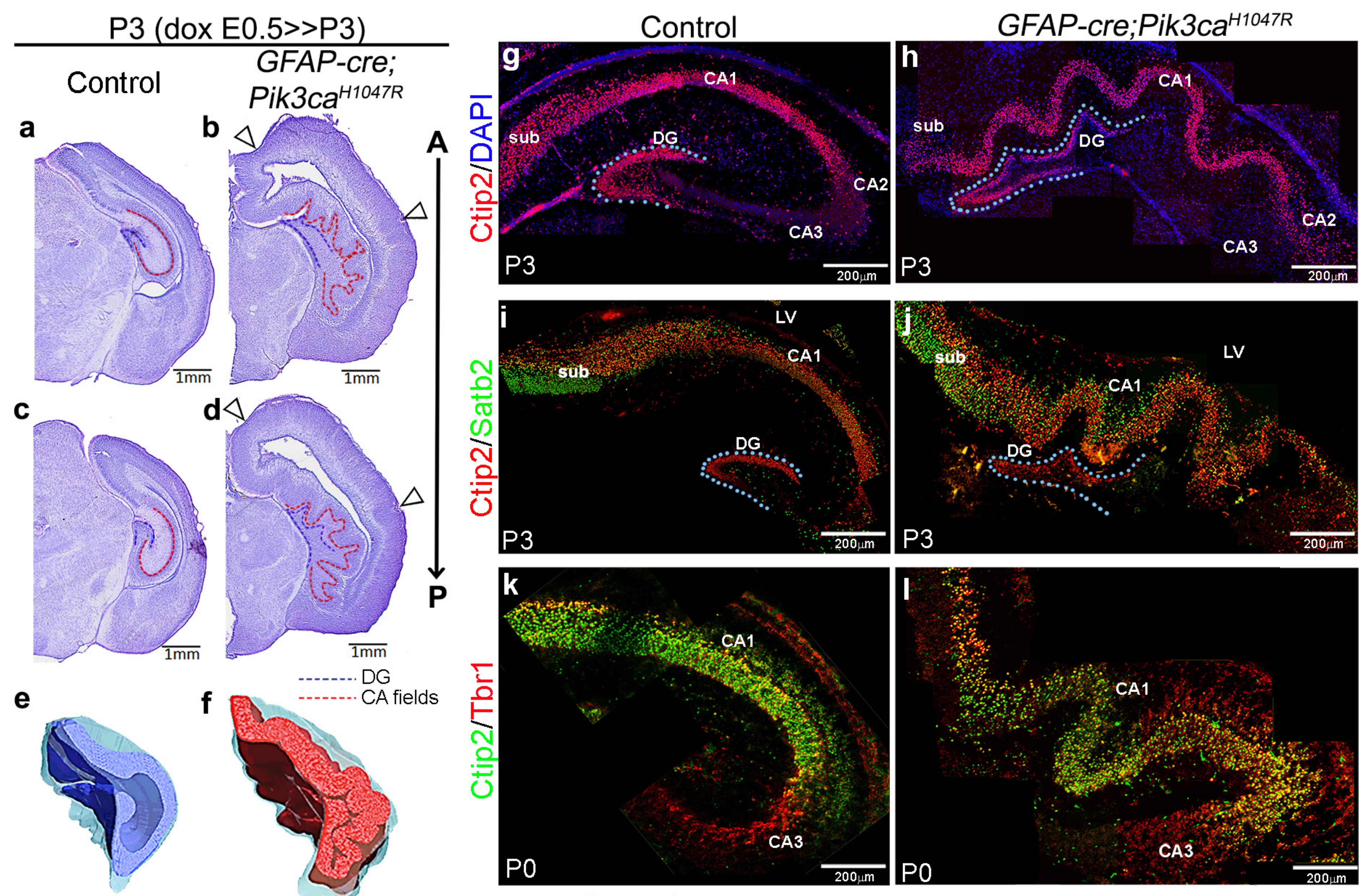
1248 **Figure 6 – Source Data 1: Significant gene list and differential expression analysis**
1249 **from P0 *Pik3ca*^{H1047R} mouse RNA-seq data**

1250 A truncated gene list is shown based on selected parameters (logFC>0.263, FDR<0.05,
1251 true for at least one biological pair comparison).

1252

1253 **Figure 6 – Source Data 2: Gene lists used in gene set enrichment analyses.**

1254 Gene lists were made based on PI3K pathway ([GO:0043491](#)), YAP pathway
1255 ([GO:0035329](#)), and the genes that are differentially expressed between the developing
1256 gyrus and sulcus in ferret, using data from [GSE60687](#) (de Juan Romero et al., 2015).



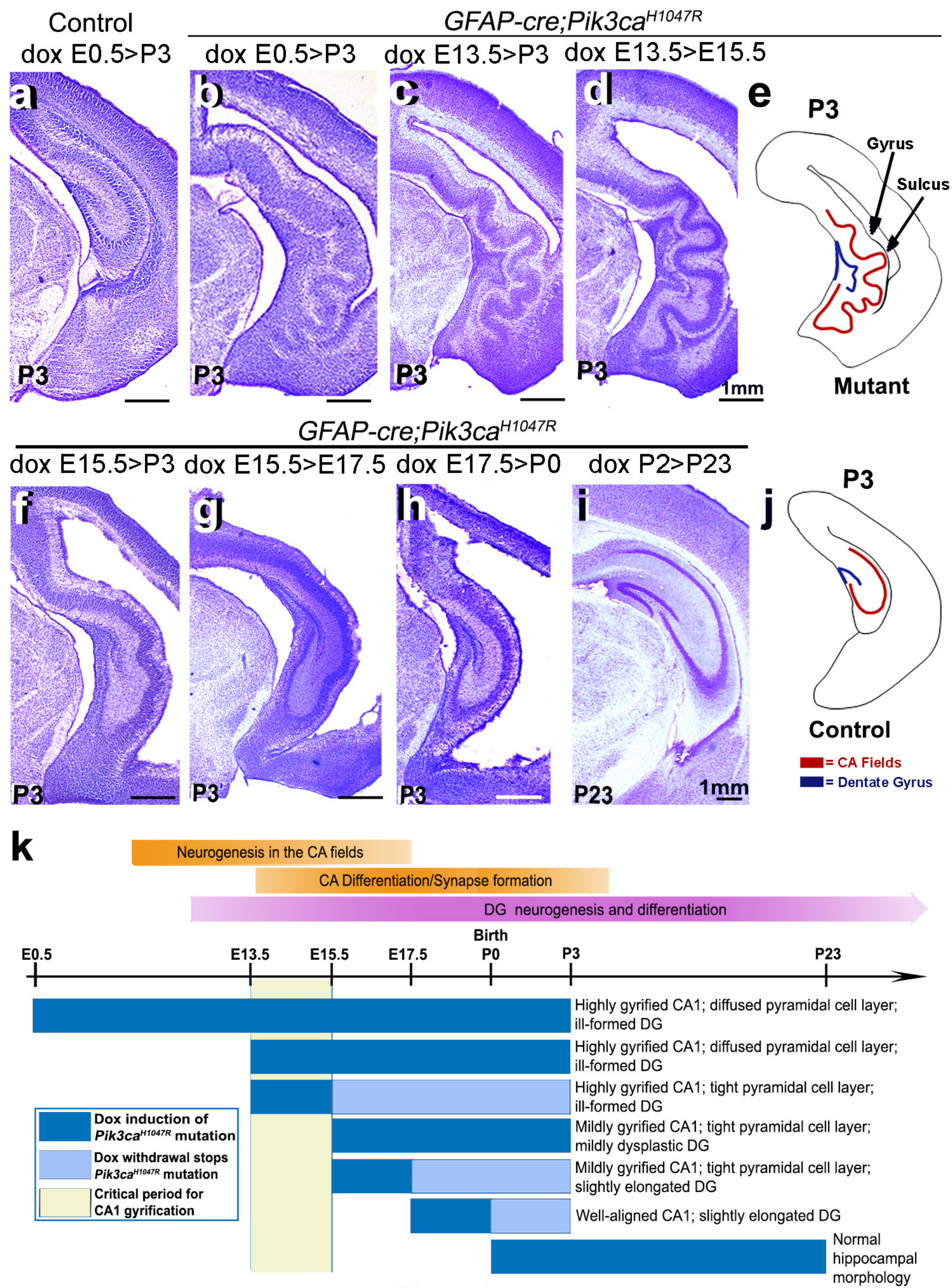


Figure 3

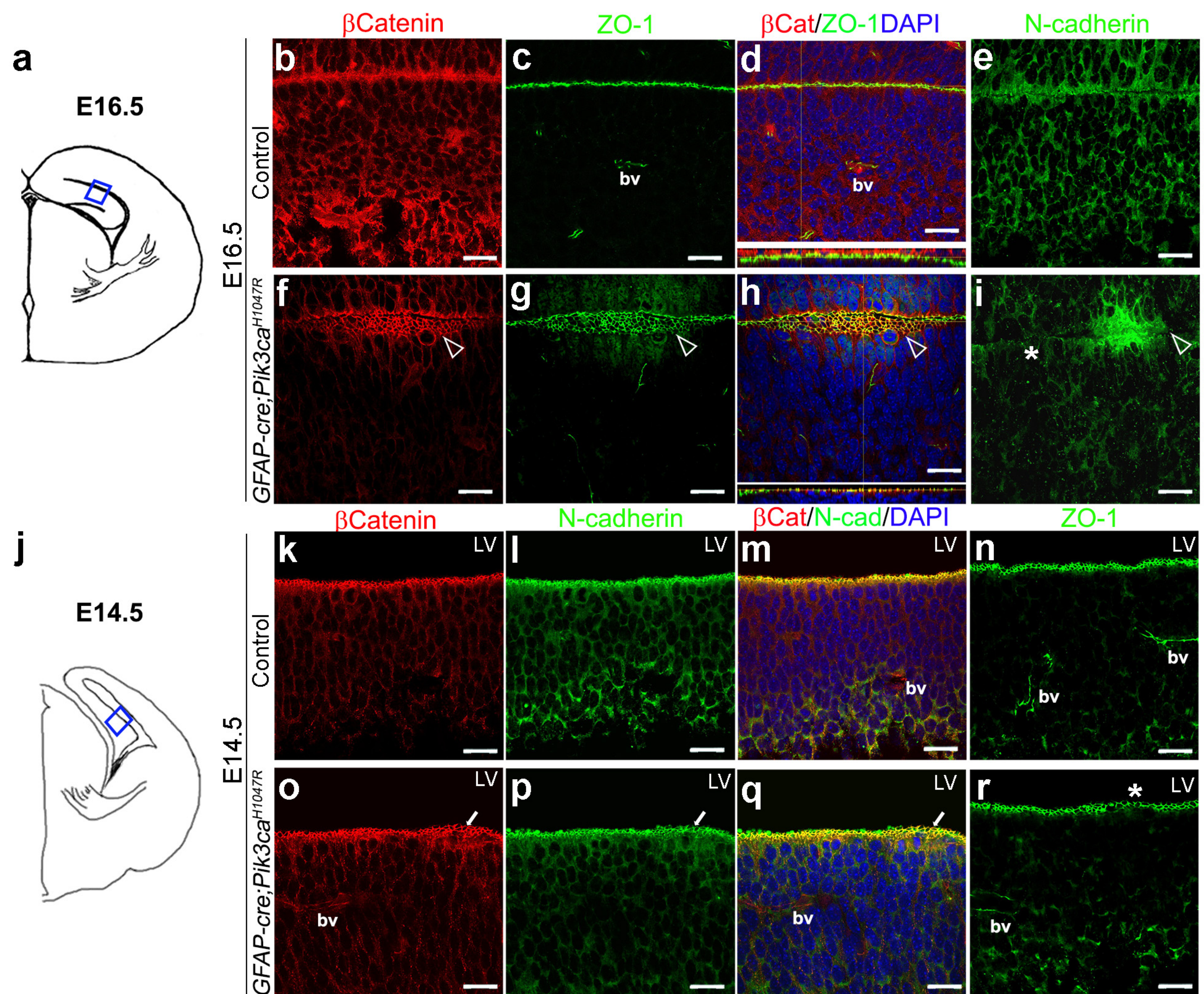
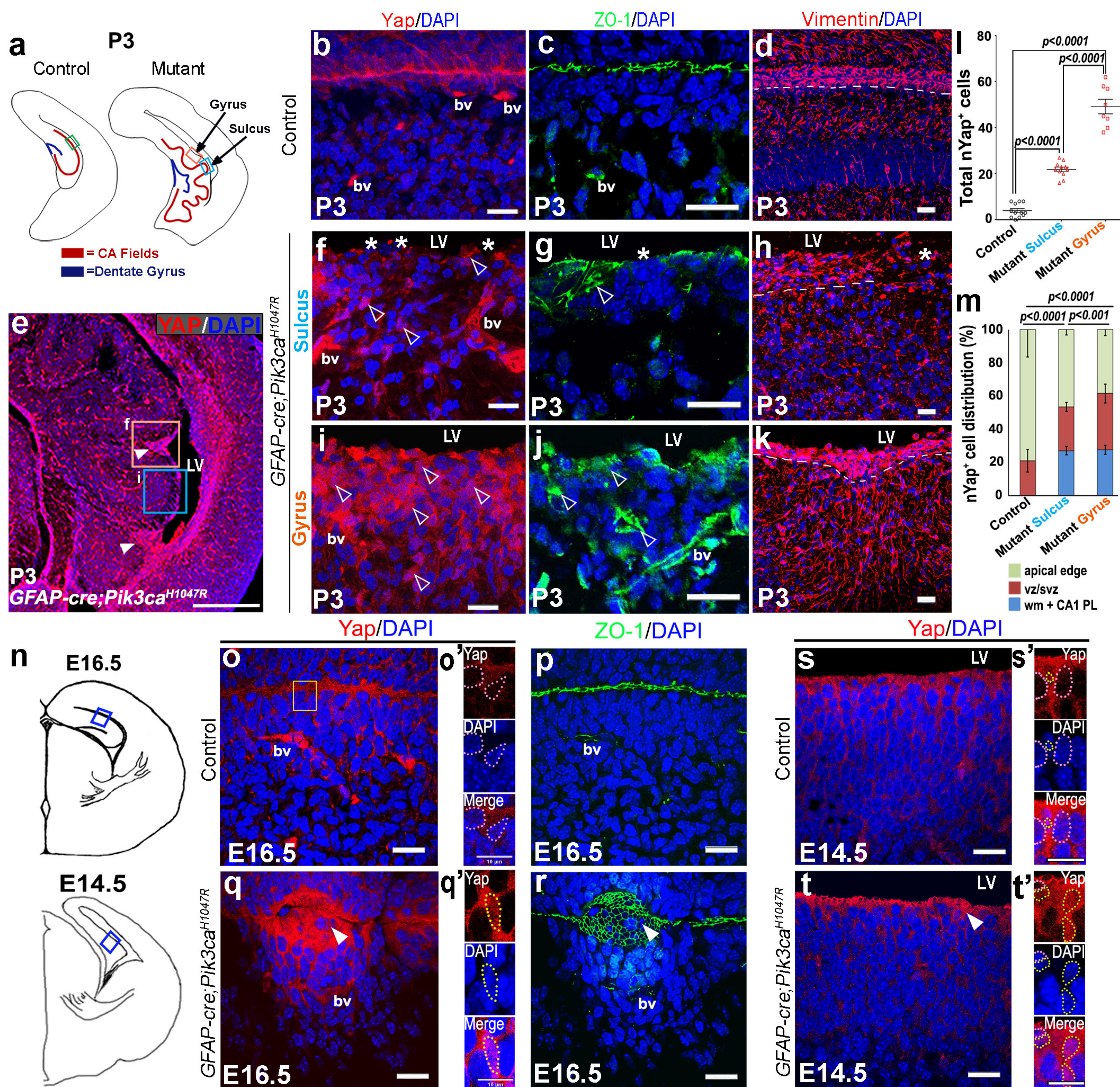


Figure 4



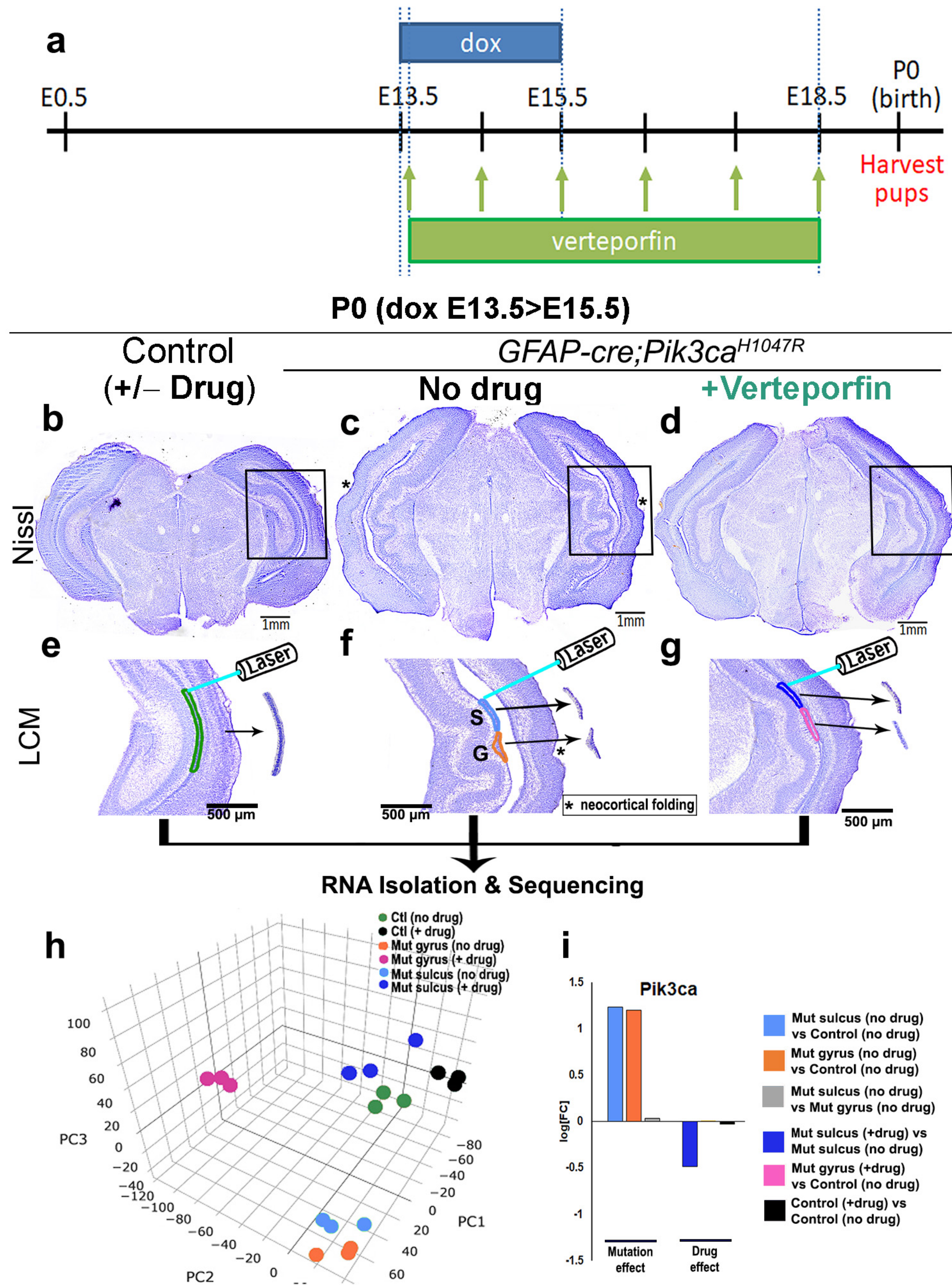


Figure 6

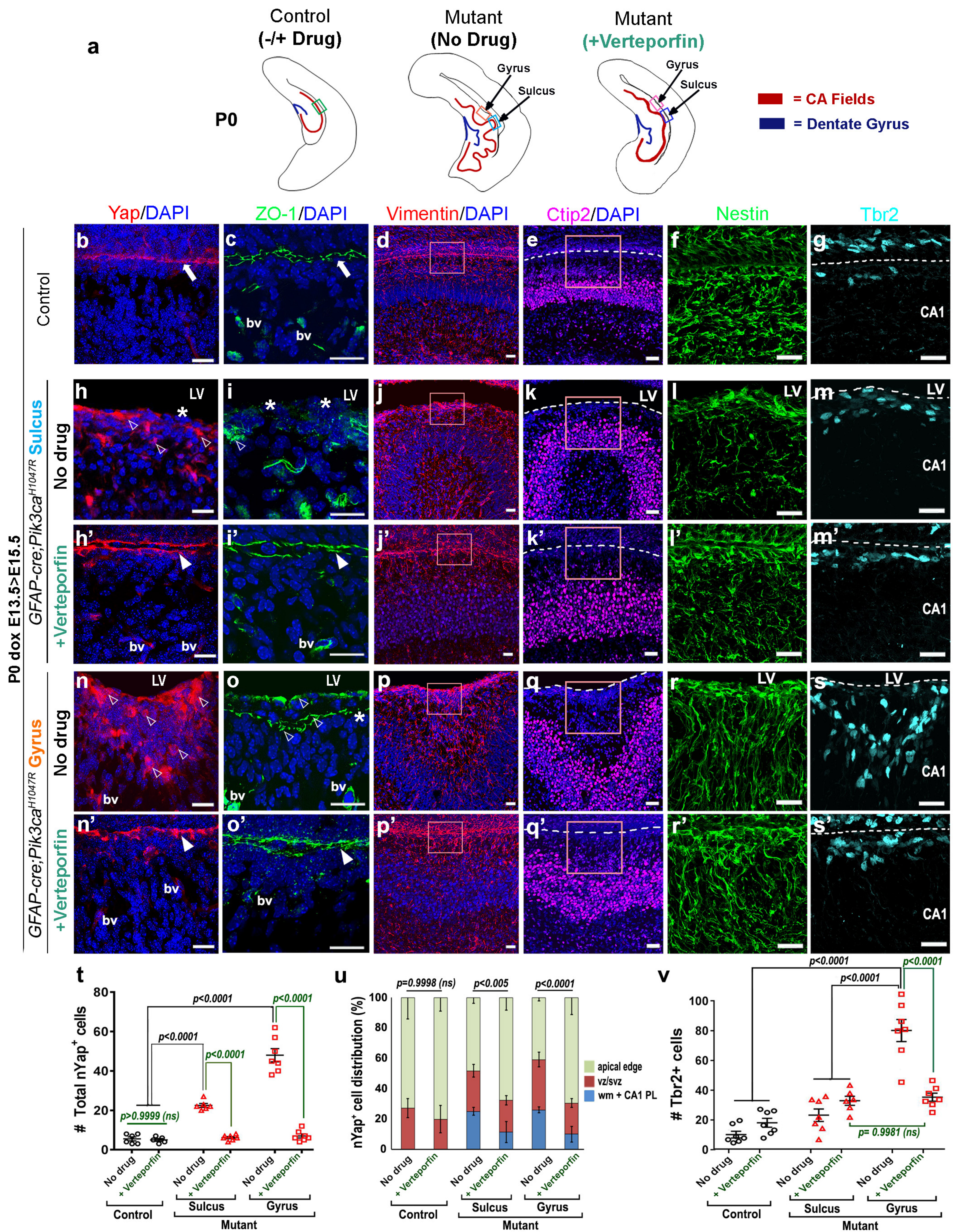


Figure 7

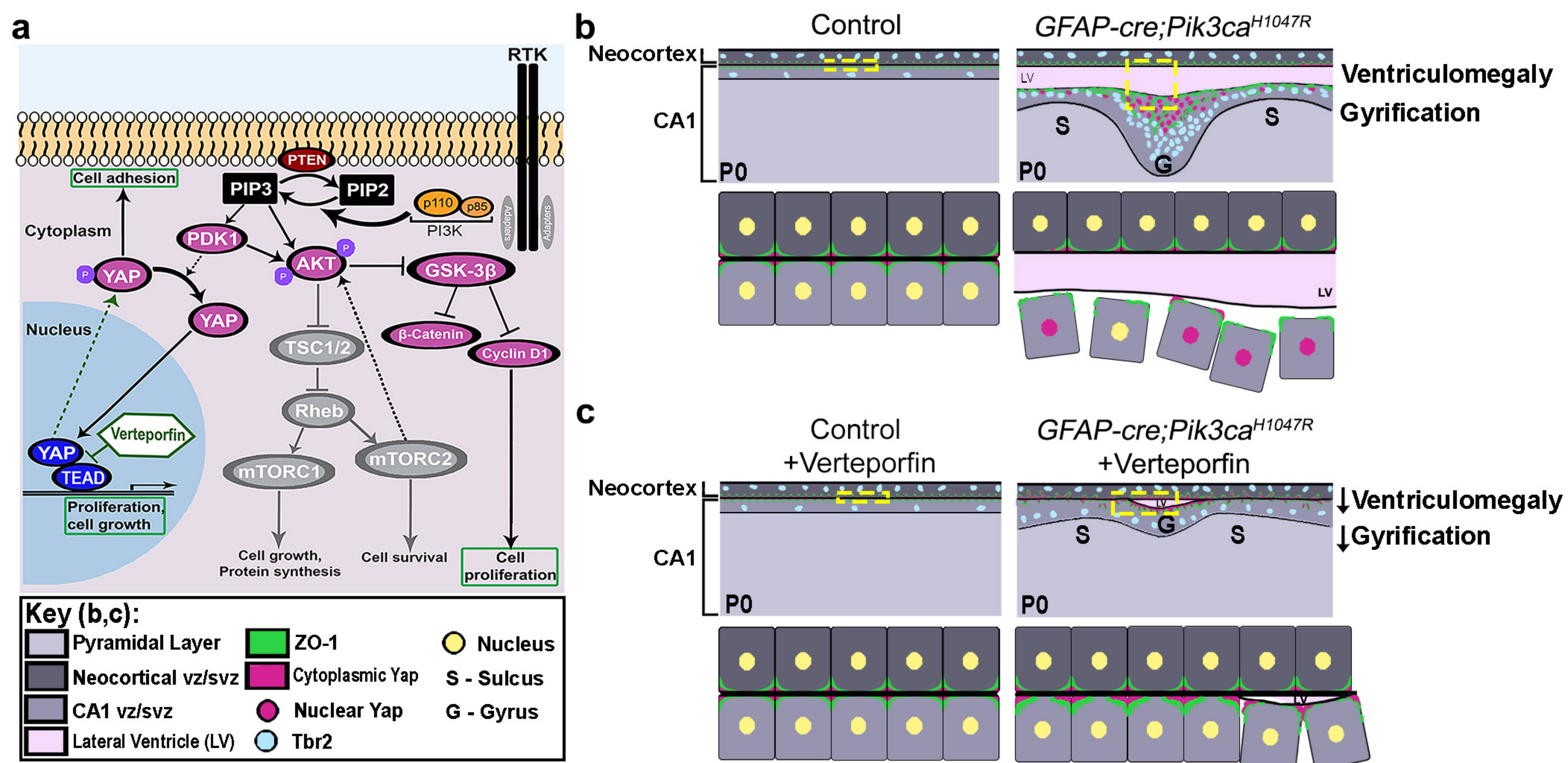


Figure 8

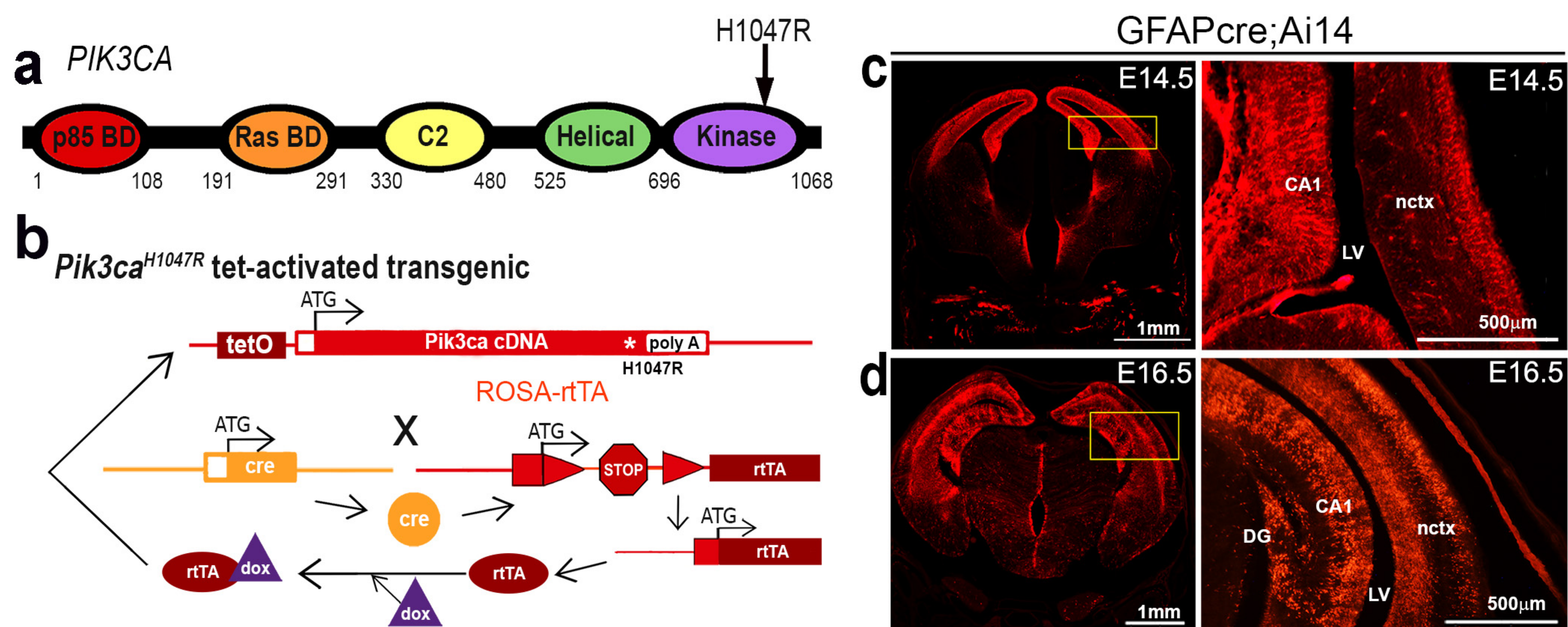
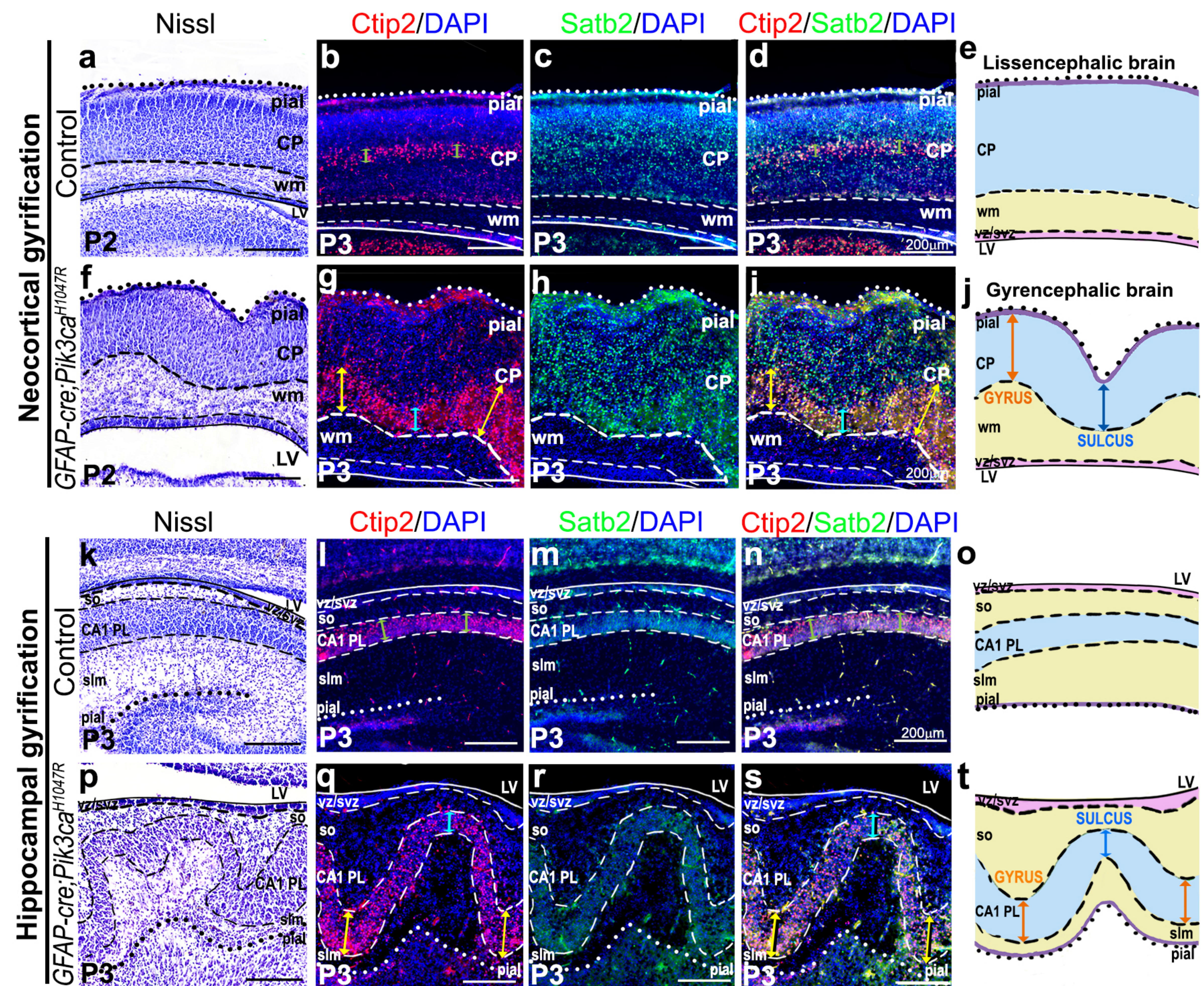


Figure 1 - figure supplement 1



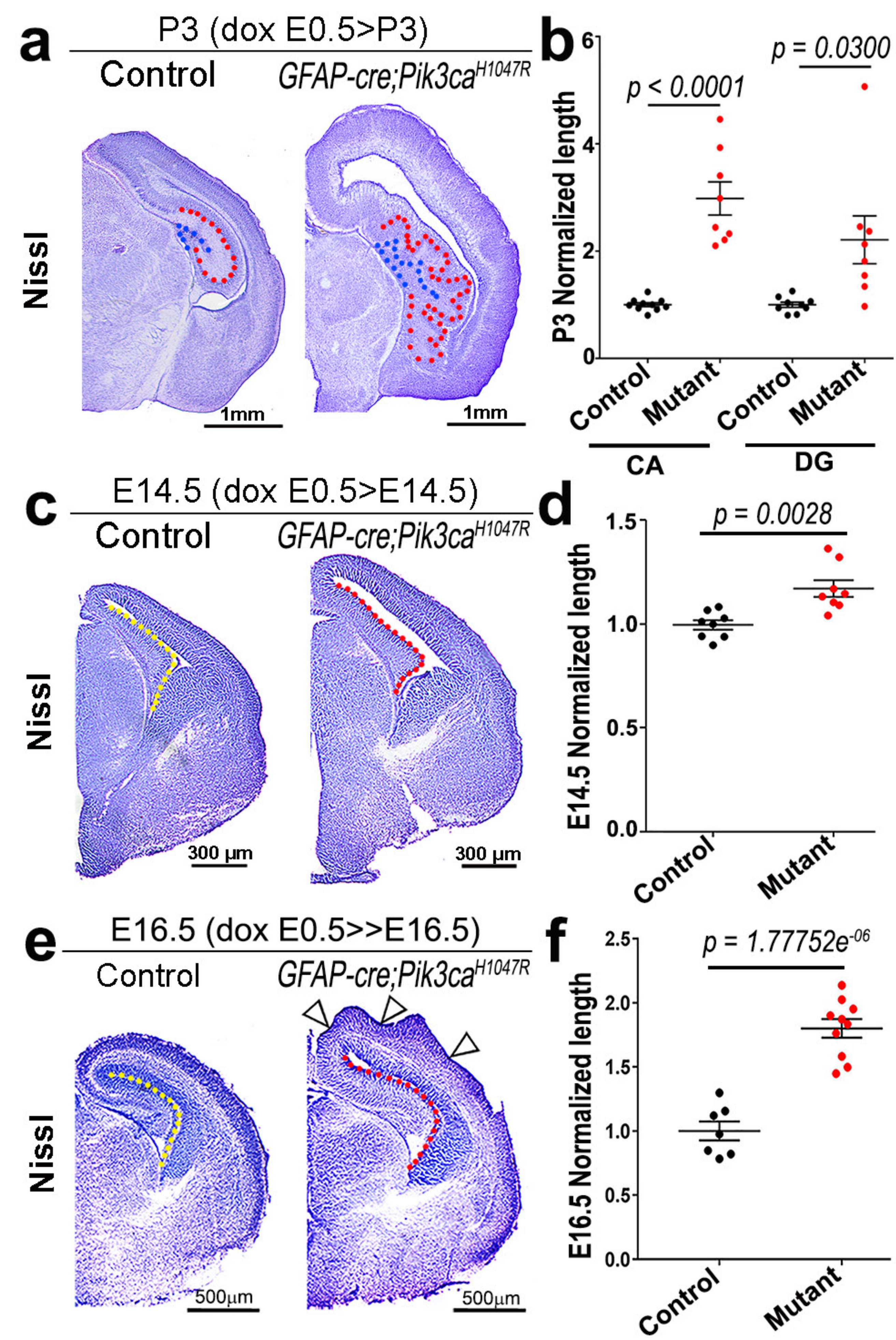


Figure 1 - figure supplement 3

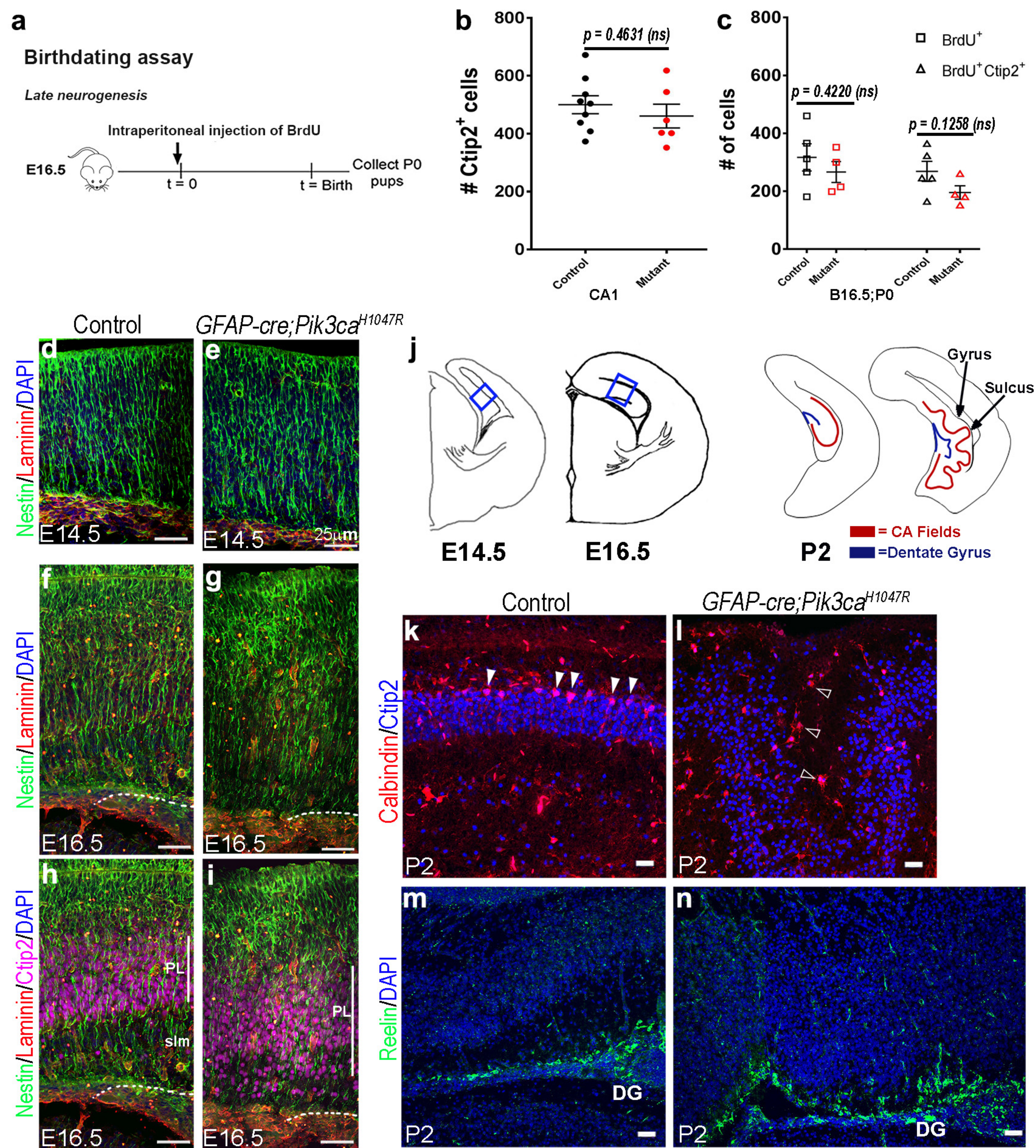


Figure 2 - figure supplement 1

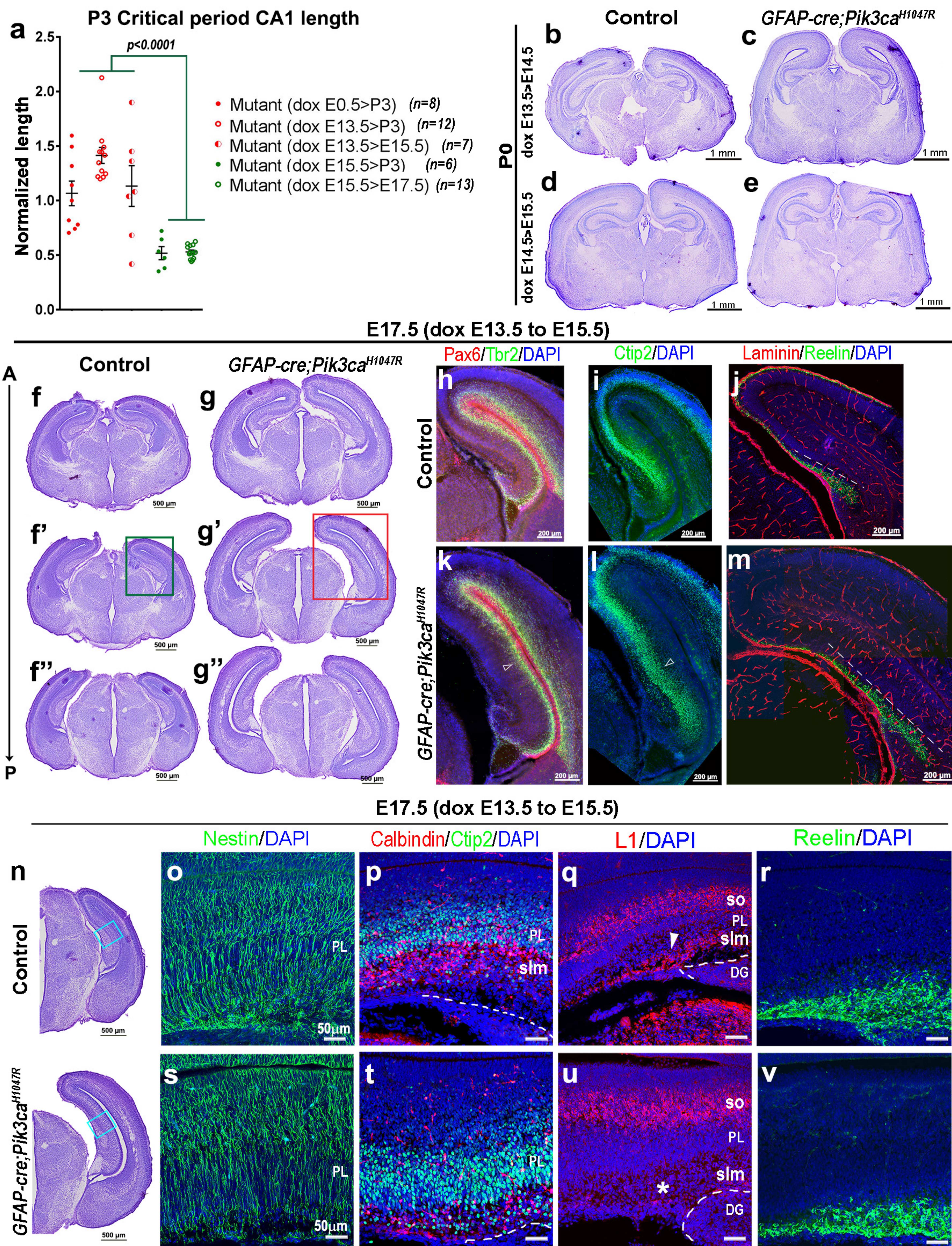
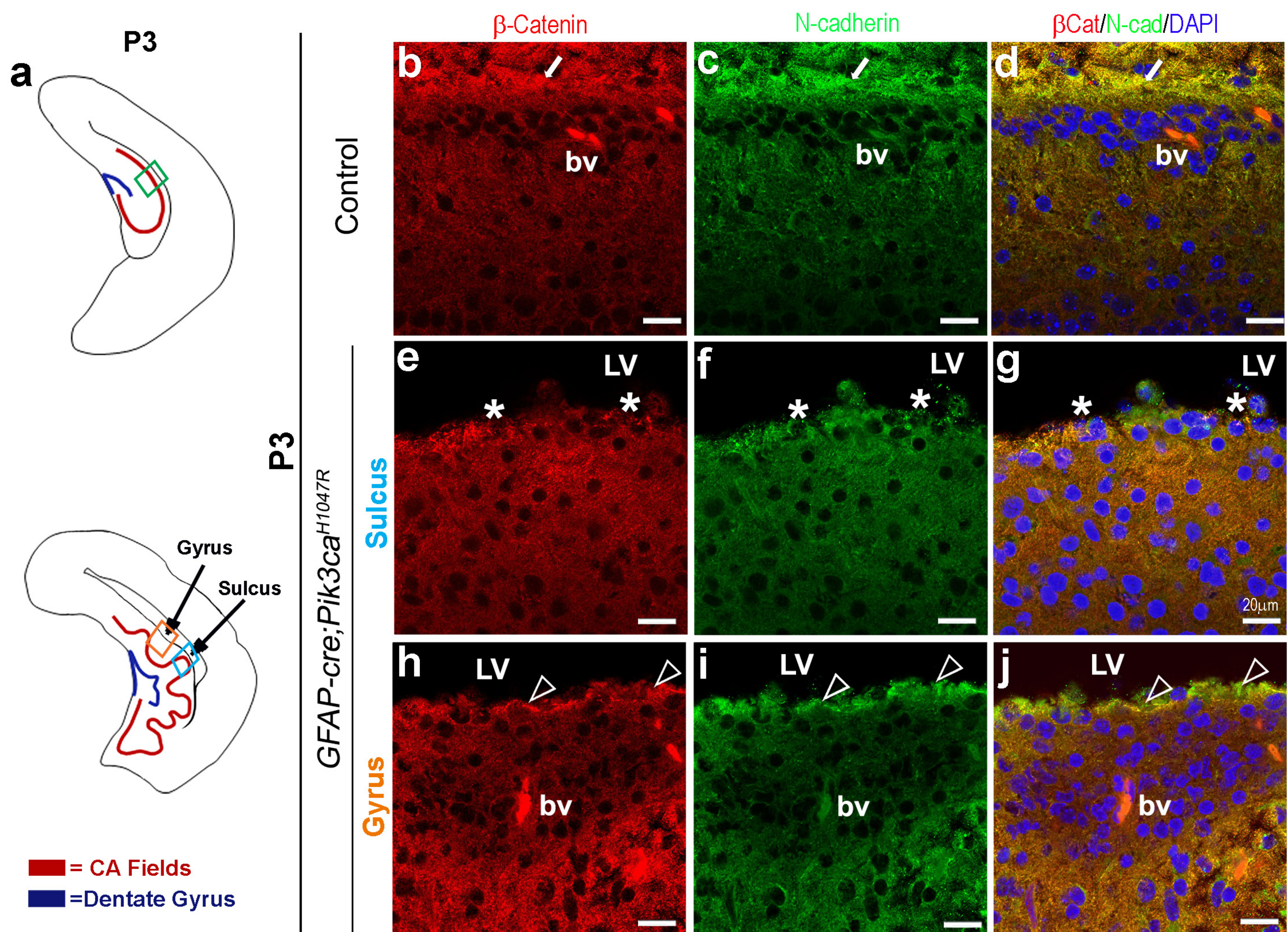


Figure 3 - figure supplement 1



P0 (dox E13.5>E15.5, NO DRUG) **Six3**/DAPI

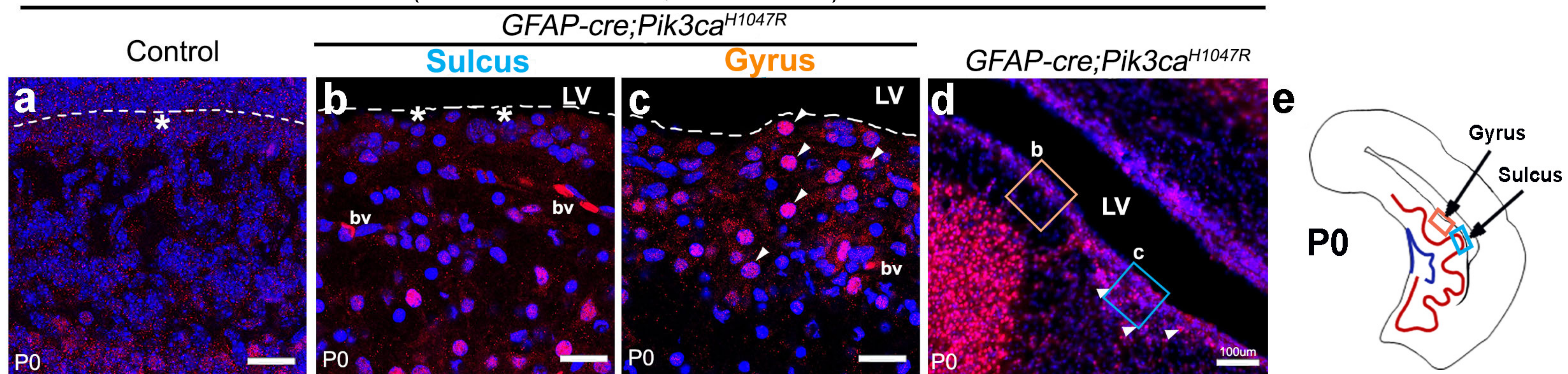


Figure 5 - figure supplement 1

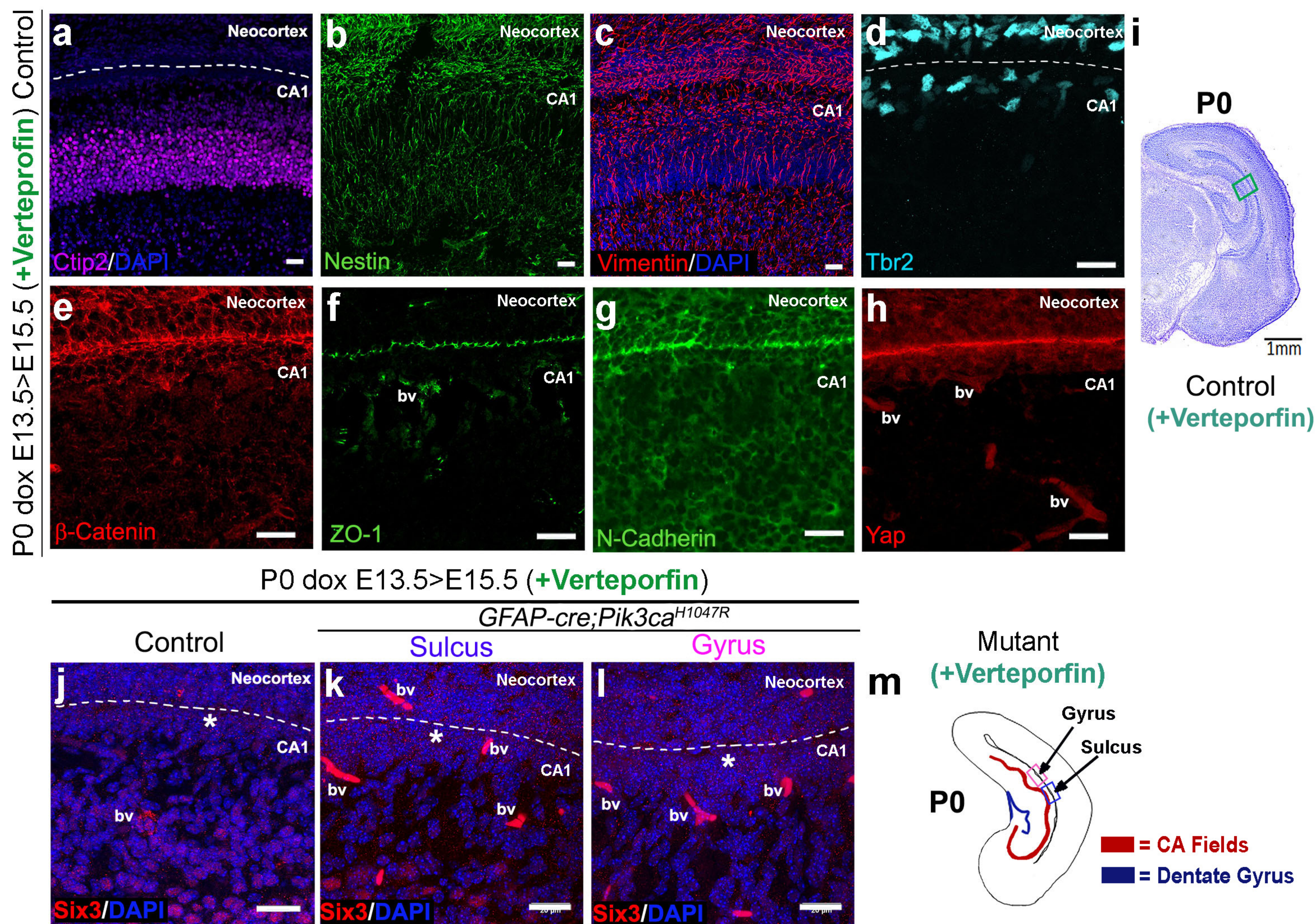


Figure 6 - figure supplement 1

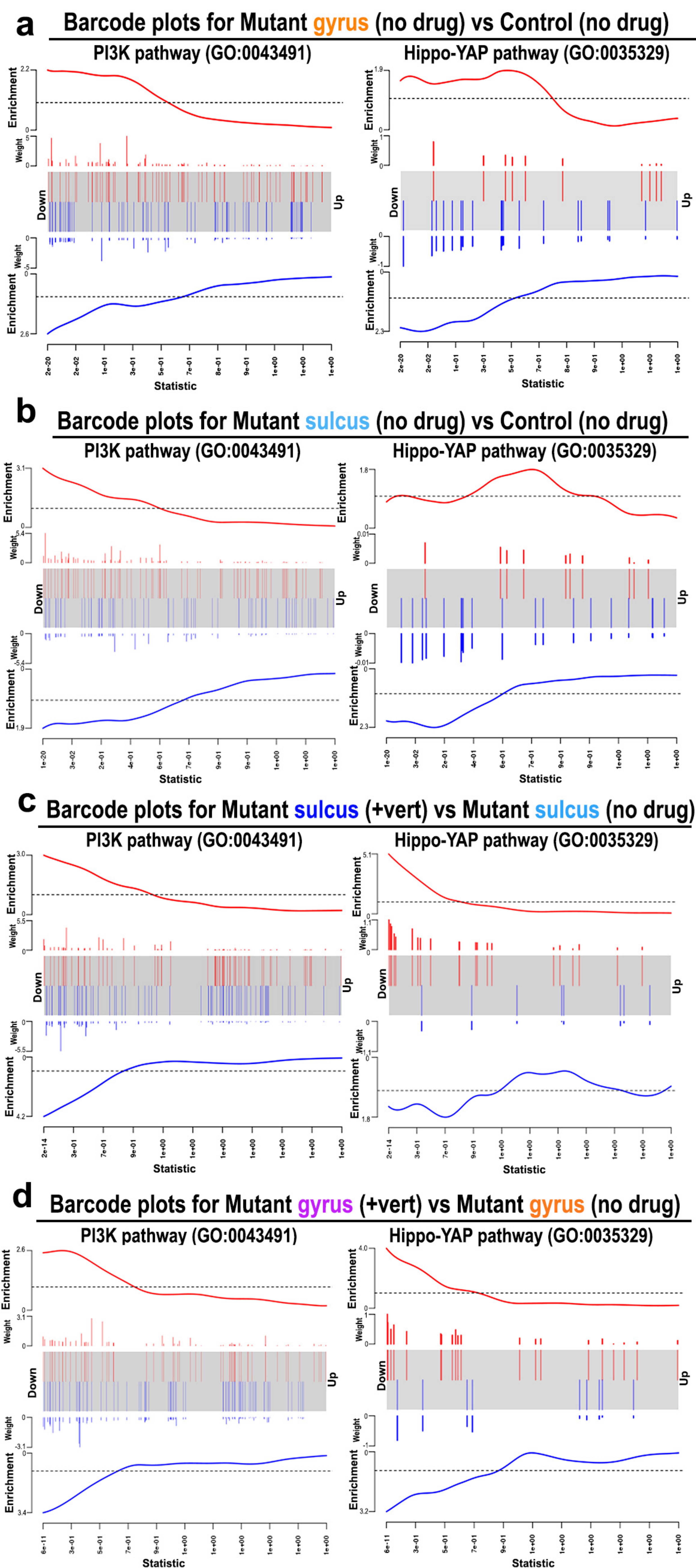


Figure 6 - figure supplement 2

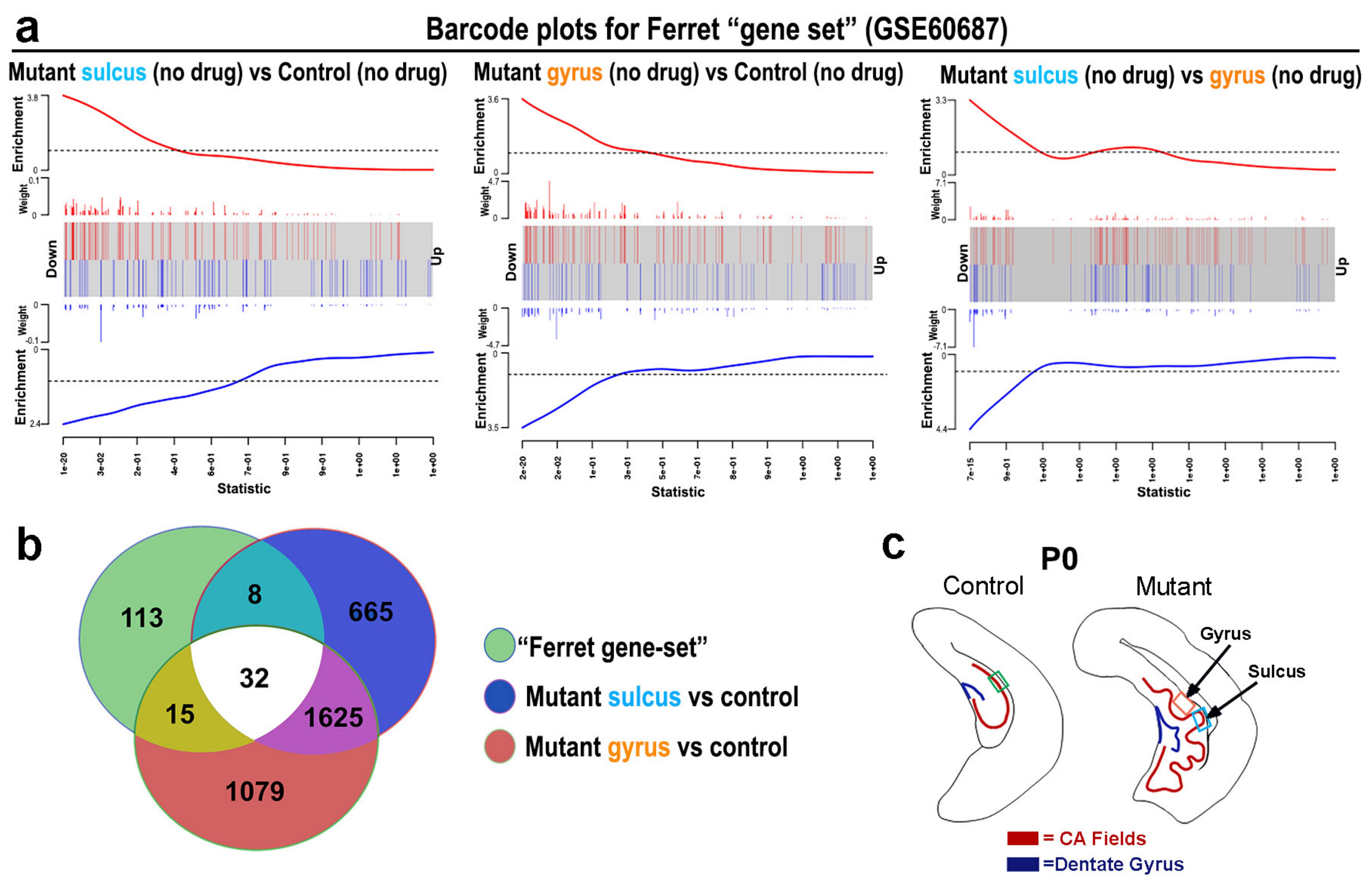


Figure 6 - figure supplement 3

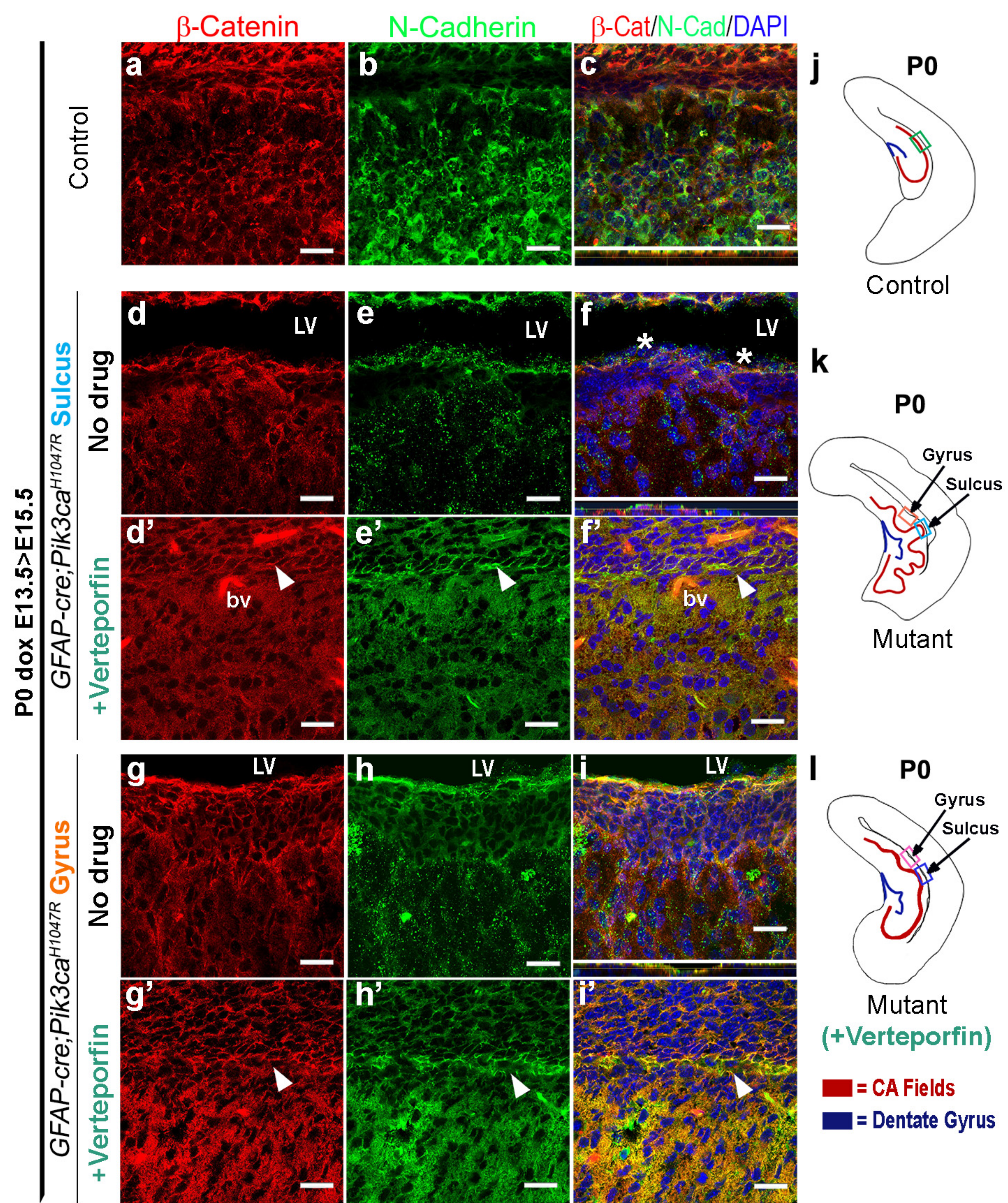


Figure 7 - figure supplement 1

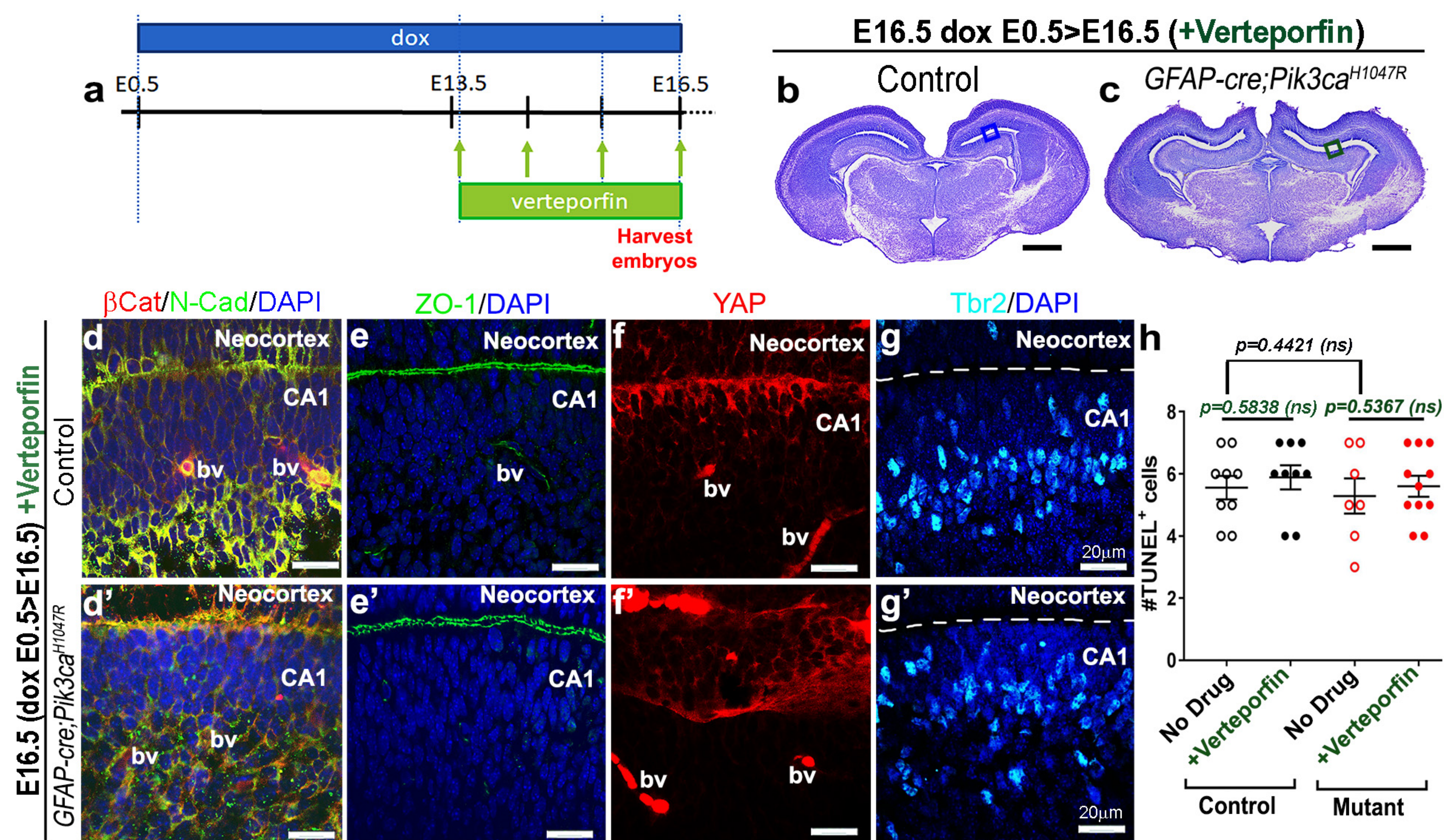


Figure 7 - figure supplement 2